Tempering of an additively manufactured microsegregated hot-work tool steel: a high-temperature synchrotron X-ray diffraction study

Eduardo B. Fonseca[1], Julian D. Escobar[2], André H.G. Gabriel[1], Giovani G. Ribamar[2], Torben Boll[3,4], Éder S.N. Lopes[1,*]

[1] School of Mechanical Engineering, University of Campinas (UNICAMP), 13083-860, Campinas, SP, Brazil

[2] Metallurgical and Materials Engineering Department, University of São Paulo (POLI-USP), 05508-010, São Paulo, SP, Brazil

[3] Institute for Applied Materials (IAM-WK), Karlsruhe Institute of Technology (KIT), Hermann-von-Helmholtz-Platz 1, D-76344 Eggenstein-Leopoldshafen, Germany

[4] Karlsruhe Nano Micro Facility (KNMFi), Karlsruhe Institute of Technology (KIT), Hermann-von-Helmholtz-Platz 1, D-76344 Eggenstein-Leopoldshafen, Germany

*Corresponding author: esnlopes@unicamp.br

Abstract

Rapidly solidified microstructures, produced by concentrated heat sources, have gained increasing attention due to the widespread expansion of additive manufacturing techniques. In laser powder bed fusion of tool steels, the as-built microstructure consists of a microsegregated network of cell-like walls decorated with retained austenite (RA). This inhomogeneous elemental distribution leads to phase transformation sequences dictated by local – instead of global – equilibrium. This work uses synchrotron X-ray diffraction to study the kinetics of retained austenite decomposition during tempering of a microsegregated as-built AISI H13 tool steel. The RA decomposition products are also characterized by hardness tests, scanning electron microscopy, and atom probe tomography. Present results evidence the formation of high temperature para-equilibrium (T < 650°C) or equilibrium (T ≥ 650°C) microstructures. The para-equilibrium microstructural path evidences isothermally stable RA, which transforms into fresh martensite upon cooling due to carbon depletion. However, the cell-like microsegregation arrangement is retained due to insufficient homogenization of substitutional elements. The equilibrium microstructural path results in isothermal transformation of RA into ferrite + carbides, as well as dissolution of the cell-like

microsegregation structure. These results provide insights towards the understanding and development of optimized heat treatment cycles appropriate for such increasingly common inhomogeneous microstructures. The results are relevant not only to laser powder bed fusion, but also to other localized melting/remelting processes with associated high cooling rates.

Keywords: powder bed fusion, AISI H13, atom probe tomography, retained austenite, martensite, heat treatment

1. Introduction

Hot-work tool steels are employed to manufacture molds and dies for applications in die casting, forging, and injection molding [1,2]. One of the most employed grades is the AISI H13 tool steel, which typically contains substantial additions of Cr (5 wt.%), Mo (1.3-1.4 wt.%), V (1 wt.%), and C (0.3-0.4 wt.%) for high-temperature microstructural stability, as well as carbide precipitation, essential for secondary hardening. Recently, the demand for complex geometries, shorter lead time, and cleaner production have stimulated the use of additive manufacturing (AM) over conventional forming and subtractive technologies [3–5]. Furthermore, AM allows strategic design of molds and dies with cooling channels that follow the tool's profile, a methodology known as conformal cooling [3,6,7]. Consequently, faster and more uniform heat extraction can be achieved, which results in increased productivity and better quality of injected parts.

The use of concentrated heat sources for AM produces a unique thermal history and consequently a microstructure which drastically differs from the one produced by the conventional and well-stablished manufacturing routes. For example, after laser powder bed fusion (L-PBF), the as-built microstructure consists of a highly segregated cellular/dendritic solidification structure, which promotes stabilization of circa 20 %-vol. of retained austenite (RA) at cell walls [8–11]. In wrought AISI H13, the amount of RA after quenching depends on the chemical composition, austenitizing temperature, and cooling rate [12,13]. However, the microstructure for tooling applications typically contains little if any RA to ensure dimensional stability of the finished parts [14].

The complete transformation of RA during tempering is essential in conventional hot-work tool steels to improve wear resistance, mechanical properties, and to provide adequate dimensional stability [15]. The thermal stability of this unconventional RA in H13 tool steels is therefore expected to be very high due to the strong segregation of Cr and Mo, initially added to the steel to guarantee high temperature stability [1,14]. Hence,

there is a current open challenge in the metallurgical field to reassess the heat treatment sequences of such highly segregated microstructures produced by additive manufacturing. Particularly, topics such as the evolution of microsegregation and the sequence of phase transformations (RA decomposition, martensite tempering, and carbide precipitation) should be revisited.

Typical heat treatment of wrought hot-work tool steels consists of austenitizing, quenching and tempering cycles, which tailor the mechanical properties to the application. The as-quenched microstructure is predominantly martensitic, with RA and carbides. The high defect density and carbon supersaturation of martensite provide the driving force for microstructural evolution during tempering, which is typically categorized into stages according to the alloying and the temperature at which the phenomena occur [14]. At room temperature and up to 200°C, short-range diffusion of carbon atoms to dislocations and martensite boundaries promotes clustering, a phenomenon known as autotempering [1,16,17]. Between 100–200°C, transition carbides precipitate within martensite as very fine particles, and are generally not associated to substitutional alloying elements, because of their sluggish diffusion at such temperature range [18]. At higher temperatures, carbide precipitation increases, forming fine and dispersed particles, which promote secondary hardening. As carbide precipitation consumes carbon, martensite loses tetragonality but retains its lath or plate morphology, being identified as tempered martensite. Above circa 600°C, in a stage called overtempering, carbides coalesce, and martensite laths or plates coarsen, while the dislocation density is reduced by recovery and recrystallization, if there is sufficient strain energy [1,19]. Simultaneously to the evolution of martensite, retained austenite also undergoes decomposition. Although RA can transform to mixtures of ferrite and carbides during tempering, in high alloyed tool steels, it remains stable during tempering and transforms to martensite on cooling [1]. Based on CCT and TTT diagrams [8,20], austenite decomposition to ferrite and carbides occurs above 600–700°C, while martensitic transformation takes place below the martensite start (M_s) temperature, in the 300–350°C range. Martensite formation is associated to carbide precipitation from austenite during tempering, which consumes carbon and locally increases the M_s temperature [14].

Up to date, most of the research efforts on additively manufactured AISI H13 tool steel have focused on applying conventional heat treatment routes designed for wrought material. Krell *et al.* evaluated several processing routes, including base plate preheating during L-PBF and post-processing heat treatments [8]. It was observed that RA decomposed after direct tempering at 500°C for 2h, and that the solidification structure only dissolved after tempering at 700°C for 2h. Both phenomena were attributed to the

poor mobility of heavier alloying elements. Åsberg *et al.* performed more complex heat treatment routes, with stress-relief, austenitization, quenching, and double tempering steps [21]. As a result, a microstructural similar to the conventional wrought material was obtained. However, high strength and ductility were only obtained when hot isostatic pressing was performed prior to austenitization. On the other hand, Yan et al. demonstrated that a change in the tempering temperature can result in a high-strength (600°C, 2h) or high-ductility (700°C, 2h) condition [22]. Previously mentioned works studied heat treatment routes of as-built microsegregated AISI H13 tool steel via *post mortem* methodologies. Alternatively, Deirmina *et al.* employed dilatometry and differential scanning calorimetry (DSC) to evaluate the transformations taking place during heat treatment [10]. It is suggested that carbides precipitate from RA during direct tempering, thus reducing the content of alloying elements, which promotes the martensitic transformation upon cooling. Simultaneously, martensite desaturation takes place, accompanied by the precipitation of secondary carbides. Although DSC and dilatometry are well-established techniques to evaluate phase transformations, the simultaneous effects of different phases can hardly be distinguished. Direct tempering without prior austenitization and quenching in parts produced by AM has shown potential to increase strength and fracture toughness, while still maintaining elevated ductility (thus increasing tool life) due to microstructural refinement during processing [22–25]. However, the unique as-built microstructure requires additional investigation to understand the transformation pathways upon different heat treatment routes, particularly regarding RA evolution.

So far, it has been clarified that RA in additively manufactured AISI H13 tool steel is abundant [8,9], even applying base plate preheating during deposition [26]. Also, it is accepted that RA is detrimental to tool service life not only because of its low mechanical strength and resistance to wear, but also because its transformation into martensite during operation may cause cracking or distortion [10,27]. Innovative heat treatment cycles can be used to favor the RA transformation into martensite. Lerchbacher *et al.* proposed reducing the dwell time of the first tempering cycle to promote the martensitic transformation, thus improving the impact toughness [13]. Subsequent tempering cycles could be used to achieve the desired performance. To this point, hypotheses have been made about the sequence of RA decomposition, carbide precipitation, and evolution of lattice defects [10,12,22], but these heavily rely on *post mortem* analyses, besides dilatometry and DSC tests. Time-resolved phase-specific techniques are thus fundamental to unveil the processes of RA decomposition and microstructural evolution

of the martensitic matrix, optimizing heat treatment routes for as-built hot-work tool steels showing a poorly homogeneous microstructure.

In this work, the authors propose a multimodal approach involving compositional and microstructural characterization to detail the phase transformations during the first cycle of tempering of a microsegregated hot-work tool steel. High-temperature *in-situ* synchrotron X-ray diffraction is used to directly explore the decomposition of RA (RA → martensite + carbides, or RA → ferrite + carbides) and the tempering of martensite (M' → ferrite + carbides). Microstructural analyses address the microsegregation and secondary precipitation via scanning electron microscopy (SEM) and compositional analyses by atom probe tomography (APT). Our observations set a basis for understanding the microstructural pathways (equilibrium or para-equilibrium) during the thermal response of these novel microsegregated microstructures commonly obtained in AM processes.

2. Materials and methods

2.1. AM deposition

Specimens for this study were produced by laser powder bed fusion using an OmniSint-160 AM machine (Omnitek) equipped with Yb:YAG fiber laser with maximum power of 400 W. AISI H13 tool steel powder was processed under Ar atmosphere, resulting in an O_2 level below 700 ppm during processing (Southland Sensing OMD-501D analyzer), using parameters determined in a previous study [11]: laser power of 172 W, scan speed of 700 mm/s, hatch space of 80 µm, and layer thickness of 30 µm. Scan strategy consisted of 5-mm strokes and a pattern rotation of 32° between layers. Baseplate preheating was not applied. The chemical composition of the AISI H13 powder purchased from Carpenter Additive is presented in Table 1.

Table 1. Chemical composition of the AISI H13 tool steel powder used in this study and the standard composition.

	Fe	C	Cr	V	Mo	Mn	Si
Powder [at.%]	Bal.	1.64	5.71	1.08	0.78	0.34	2.02
Powder [wt.%]	Bal.	0.36	5.44	1.01	1.37	0.34	1.04
Standard [wt.%]	Bal.	0.32–0.40	5.13–5.25	1.0	1.33–1.40	---	1.0

2.2. *Ex-situ* heat treatments

Heat treatments were performed in cylindrical specimens with 5 mm in diameter and 10 mm in height, which were built with their longitudinal axis parallel to the build direction. Heat treatment routes consisted of direct tempering in air in an electric resistance furnace at 550, 575, 600, 625, and 650°C for 1h.

2.3. Microstructural characterization

As-built and tempered specimens were sectioned in half (mid-length) for metallography and prepared using conventional grinding and polishing techniques, using 1 µm diamond paste and 0.02 µm colloidal silica. Finally, samples were etched with 5% Nital solution and analyzed in SEM using a ThermoFischer Quanta 650 and etched with Vilella's reagent and analyzed in a Zeiss Evo MA 15. Scanning transmission electron microscopy (STEM) was performed on a thin lamella extracted from the as-built specimen using focused ion beam (FIB) lift-out procedure in a ThermoFisher Helios NanoLab 660. High-angle annular dark-field (HAADF-STEM) analysis was performed in a JEOL JEM-2100F microscope operating at an accelerating voltage of 200 kV. Vickers hardness tests were performed on polished surfaces using a LECO LMV-50V automatic tester, with a load of 0.3 kgf for 15 s. At least 18 measurements were performed in each sample, and average values are presented along with a confidence interval of 95%.

2.4. *In-situ* heat treatments

2.4.1. Apparatus

High-temperature *in-situ* synchrotron X-ray diffraction (HTXRD) analyses were performed on bowtie specimens (dimensions provided in Supplementary Material Fig. S1) built in XZY orientation. The surface was polished with 1 µm diamond paste prior to characterization. The experiments were performed at the X-ray Thermo-Mechanical Scattering (XTMS) experimental station of the Brazilian Synchrotron Light Laboratory (LNLS/CNPEM). A beam energy of 12 keV (1.033202 Å) illuminated an area of 2 x 0.5 mm on the specimen's surface (schematically shown in Supplementary Material Fig. S1). The installation consisted of an X-ray diffraction beamline working in reflection mode, coupled with a Gleeble 3S50 thermomechanical simulator and a heavy-duty goniometer, where X-ray detectors were mounted. The thermomechanical simulator controlled the specimen temperature via type-K thermocouples discharge-welded to the center of the reduced section. The collected X-ray diffraction data allowed time-resolved tracking of

phase transformations along a predetermined heat treatment. The programmed thermal cycles were similar to the *ex-situ* furnace heat treatments and are schematically described in Fig. 1.

2.4.2. Measurement conditions

Specimens were heated to isothermal tempering temperatures at a constant rate of 0.833°C/s and held for 4200 s, followed by cooling to room temperature at a rate of 3°C/s, which simulates forced-air cooling conditions. During heating and isothermal plateau, specimens were kept under vacuum. Upon cooling, the chamber was filled with argon gas to achieve the desired cooling rate. A continuous heating (CH) experiment was conducted from room temperature up to 950°C to evaluate the temperature-dependent RA stability in the subcritical and intercritical fields.

X-ray diffraction was collected in two modes: continuous and full scan. A schematic representation of the X-ray diffraction collection modes is indicated in Fig. 1. Full scans were acquired before heating the specimen (as-built full scan), by the end of the isothermal plateau (full scan before cooling), and after cooling the specimens to room temperature. These were performed by moving the goniometer in a step-by-step fashion to obtain a broad diffractogram including the FCC-phase (γ-austenite) {111}, {200}, {220}, {311}, {222}, {400}, {331}, {420}, and {422} peaks and the BCC-phase (α-ferrite and M'-martensite) {110}, {200}, {211}, {220}, {310}, {222}, and {321} peaks.

On the other hand, continuous scans were collected with the goniometer in a fixed position, observing a smaller 2θ range, including the FCC-phase {111}, {200}, and {220} and the BCC-phase {110} and {200} peaks, thus allowing faster sampling rates. During heating and cooling, fast diffraction sampling was conducted with an exposure time of 6.0 s; while during the isothermal plateau, the exposure time was 66.7 s. A continuous acquisition sequence was used, allowing for less than 0.5 s of read-out time within consecutive measurements. A 2D detector (Rayonix SX165) was used to acquire the diffraction patterns during the tempering cycles at 550, 580, and 600°C and during the CH experiment. The tempering cycle conducted at 650°C involved two linear detectors (Mythen-1K), with exposure time of 10.3 s between consecutive collections.
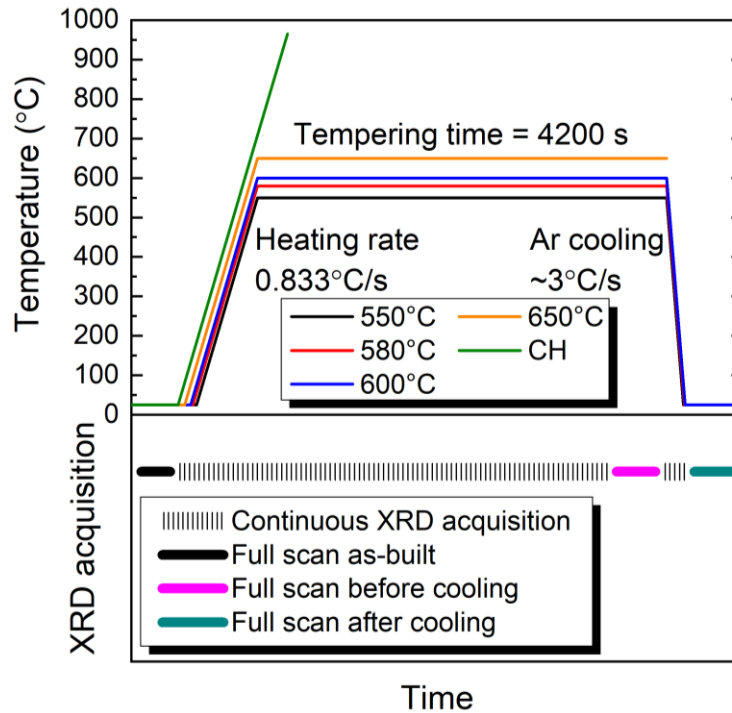
Fig. 1. Heat treatment cycles studied during high-temperature *in-situ* synchrotron X-ray diffraction. The X-ray collection modes and the sequence of X-ray data collection are shown in the lower panel of the figure. The tempering time of 4200 s corresponds to 3600 s in continuous acquisition mode and 600 s for a full-scan acquisition. CH: continuous heating.

2.4.3. Data processing

The 2D detector files were processed using Dracon, a MatLab-based software developed for users of the XTMS beamline. The process consisted of calibrating the detector and sample positions, and integrating the 2D Debye-Scherrer rings in the azimuthal angle to obtain typical intensity versus diffraction angle plots. Calibration was performed with Y_2O_3 powder, measured using the same acquisition setup. The diffractograms were processed using automatic profile fitting tools for large-scale batch processing, allowing the fitting and subsequent extraction of peak position, area under the peak, and full width at half maximum (FWHM) of the available BCC- and FCC-phase peaks.

For each measured sample, lattice parameters and FWHM values were normalized by the corresponding initial as-built values. Thus, a/a_0 and $FWHM/FWHM_0$ values are reported. The BCC {110} and FCC {111} peaks are partially convoluted, and therefore were not considered for lattice parameter or FWHM analysis. Instead, the BCC ferrite/martensite {200} and FCC retained/reverted austenite {200} peaks were used. The

8

volume fraction of austenite was calculated using the Averbach–Cohen method, as described in [28–30].

2.5. Atom Probe Tomography

APT was carried out to study the elemental distributions in the as-built condition and after tempering at 575°C for 1h in furnace. Tips for APT were obtained by cutting the cylindrical specimens into 0.3 x 0.3 x 10 mm wires using a wire saw, which were then clamped to a copper holder. The wires were electropolished in two steps, first to form a neck and the final step to form the tip by separating both ends. Hence, the APT tips were obtained from the mid-length of the cylindrical specimens. The first electropolishing step was performed using a solution of 10%-vol. perchloric acid in acetic acid and a potential of 13–17 V between the wire sample and the counter electrode platinum ring. The final electropolishing step was performed using a solution of 2%-vol. perchloric acid in acetic acid and a potential of 14–15 V between the wire sample and a flat platinum counter electrode.

A CAMECA LEAP 4000X HR was used in laser mode with a pulse rate of 100–200 kHz, pulse energy of 50 pJ, tip temperature of 50 K, and detection rate of 0.5–1.0%. Tip reconstruction and analysis were performed in IVAS software, version 3.6.14. At least three tips were analyzed for each condition. Carbon-based isosurfaces were calculated to highlight martensite/RA interfaces. Additionally, 2D concentration heat maps were constructed from cubic regions of interest (ROIs) with 25 nm thickness. Local compositional analyses at the RA and martensite portions of the microstructure were performed after deconvolution of overlapping peaks in the mass spectrum, such as $^{12}C^+$ and $^{12}C^{12}C^{++}$ at 12 Da, and $^{12}C^{12}C^+$ and $^{12}C^{12}C^{12}C^{12}C^{++}$ at 24 Da. Deconvolution of overlapping peaks was performed based on the natural abundance of the isotopes and taking into account the peaks of $^{13}C^+$ at 13 Da, $^{12}C^{13}C^{++}$ at 12.5 Da, $^{12}C^{13}C^+$ at 25 Da, and $^{12}C^{12}C^{12}C^{13}C^{++}$ at 24.5 Da. Cluster analyses were performed in the martensitic regions of the APT tips using the tenth nearest neighbor distributions for C, V, Cr, and Mo.

3. Results

3.1. Microstructural characterization before and after tempering

The microstructure of the as-built and furnace heat-treated samples are shown in Fig. 2, along with their corresponding Vickers hardness. The microstructure of the as-built sample is a result of fast solidification during AM and consists of a cellular/dendritic

solidification structure, which is effectively revealed by the Nital etch. Martensite was the main microconstituent, and noticeable martensitic blocks are indicated by the yellow arrows in the insert images obtained with Vilella's etch (inserts in Fig. 2). RA is also present and preferably found at cell walls, as reported in the literature [8,10,11], leading to an as-built hardness of 564 ± 13 HV. Lath martensite can be observed in the STEM-HAADF images in Fig. 3, along with small carbides. Carbide precipitation has been reported in AM of tool steels due to element partitioning, particularly C, Cr, V, and Mo [11,21,31].

The cellular/dendritic solidification structure is retained after tempering at 550 and 575°C, while it partially degenerates after tempering at 600 and 625°C. At 650°C, the solidification structure is mostly erased, while the remaining cell walls become thinner. The martensite blocks (indicated by yellow arrows in Fig. 2) observed in the as-built condition and in the tempered specimens between 550 and 625°C are no longer visible in the specimen tempered at 650°C. Moreover, the presence of carbides (red arrows in Fig. 2) indicates that overtempered martensite is the main microconstituent of the specimen tempered at 650°C. Carbides are also found along prior cell walls, and grain boundaries are decorated with a carbide network. An overall increase in hardness was observed after tempering in the range between 550 and 625°C, achieving a peak of 651 ± 5 HV at 575°C. At 650°C, a considerable decrease in hardness to 487 ± 3 HV occurred, which is below the hardness of the as-built condition. The tempering curve is provided in the Supplementary Material, Fig. S2.
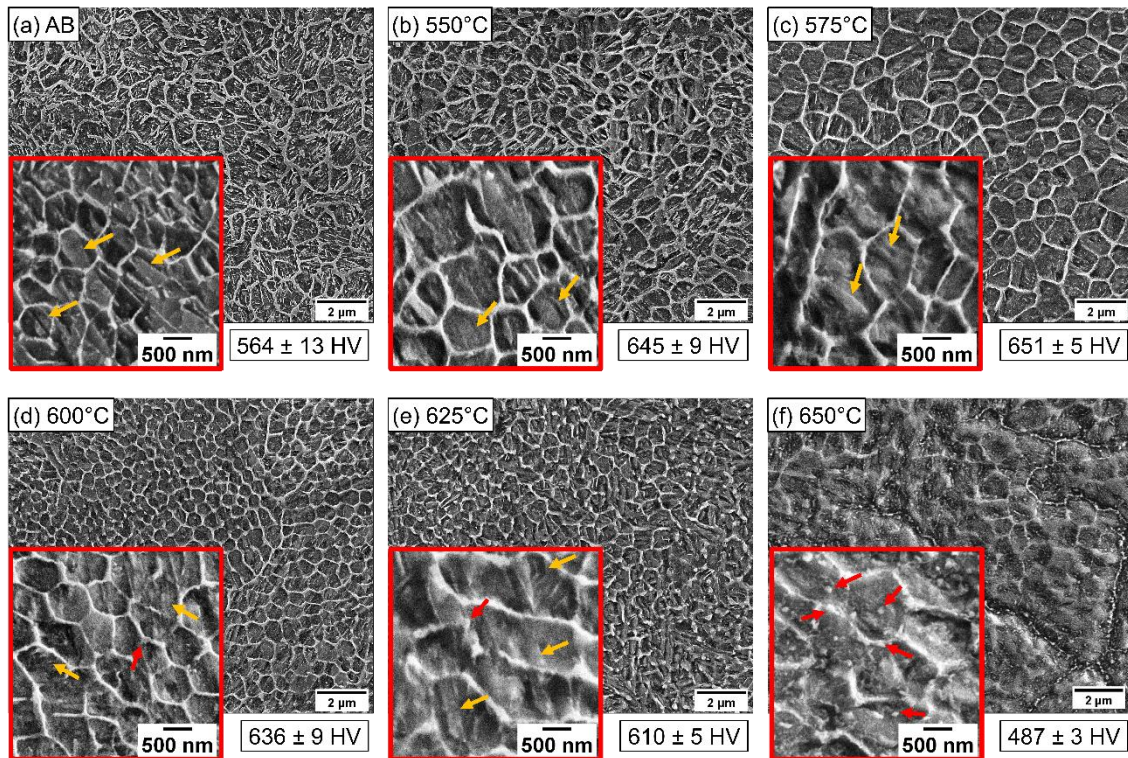
Fig. 2. Micrographs obtained by SEM-SE and Vickers hardness ($HV_{0.3/15}$) values of the (a) as-built (AB) and (b-f) tempered specimens at (b) 550°C, (c) 575°C, (d) 600°C, (e) 625°C, (f) 650°C. Low magnification images: Nital etch, high magnification inserts: Vilella's etch. Yellow arrows: martensite blocks, red arrows: carbides.
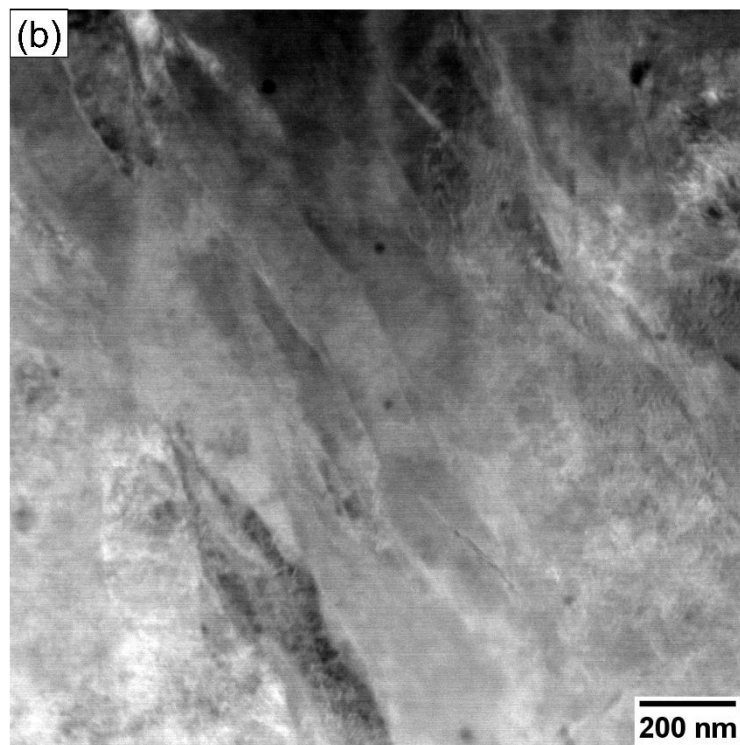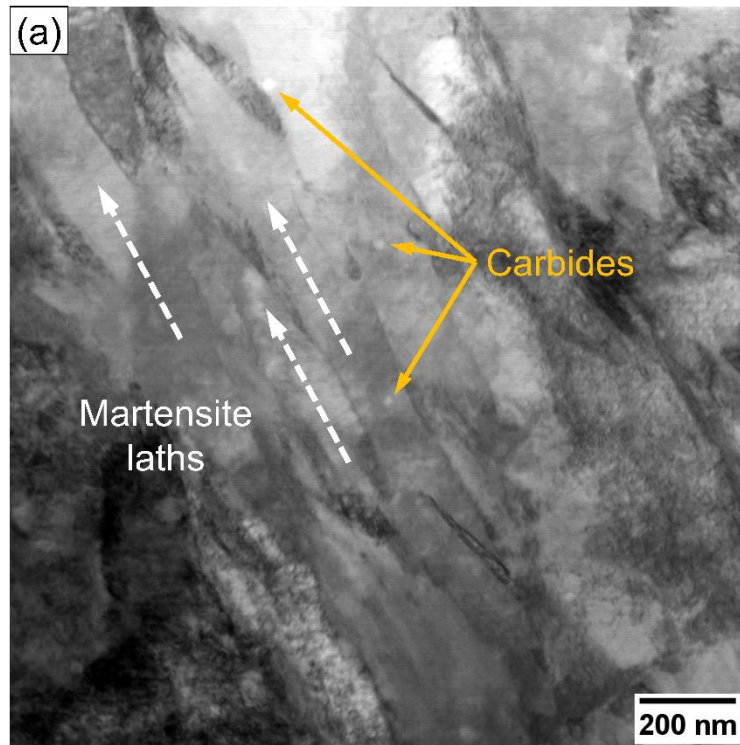
Fig. 3. (a) Bright field and (b) HAADF-STEM images of the as-built AISI H13 tool steel showing martensite laths and carbides.

3.2.   High-temperature *in-situ* heat treatments

Representative diffractograms obtained in the HTXRD experiments are presented in the Supplementary Material in Fig. S3. Based on previous characterization [11], the as-built BCC peaks are initially regarded as martensite peaks, thus assuming that ferrite formation during L-PBF is either negligible or absent. Carbide peaks were not identified in the diffractograms due to limitations of the XRD technique regarding the volume fraction of carbides, assumed to be below 2%-vol. Thus, carbides were not considered in the phase fraction calculations.

3.2.1. Decomposition of RA during heating stages

Fig. 4a-b show the temperature- and time-resolved evolution of the austenite volume fraction, respectively, obtained from HTXRD. The starting volume fraction of RA ranged between 20 and 26%-vol. among 5 analyzed samples. Slight decrease in RA occurs in all cases during the heating stage of the tempering cycles, as shown in Fig. 4a. Additionally, sluggish decomposition of RA occurs upon continuous heating up to 743°C, followed by a fast decrease, reaching a minimum of 17%-vol. near 840°C. Above this temperature, sharp austenitization occurs, indicating that the microstructure has reached the intercritical range ($A_{c1} - A_{c3}$). The equilibrium A_{e1} and A_{e3} temperatures for the AISI H13 tool steel are expected at 865°C and 904°C, respectively, according to ThermoCalc calculations using the TCFE9 database. The experimental results show anticipated austenitization and delayed complete austenitization compared to thermodynamic equilibrium conditions.
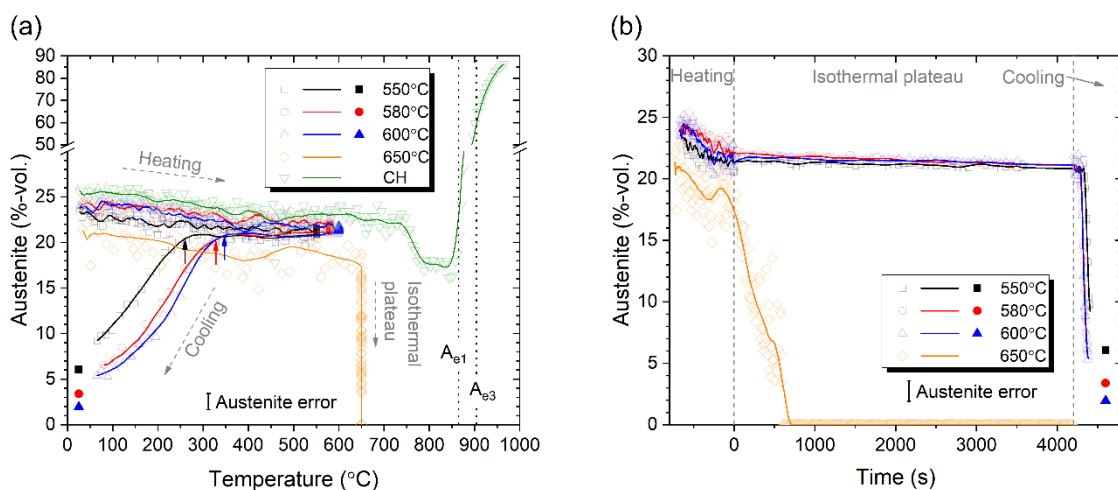

Fig. 4. Evolution of the austenite volume fraction in as-built AISI H13 tool steel measured by HTXRD during different tempering cycles: (a) temperature-resolved, and (b) time-resolved austenite dissolution. Hollow symbols are experimentally retrieved points.

Continuous lines were obtained after smoothing the experimental points by a weighted moving average method. Solid symbols correspond to full scan measurements. A time offset in (b) was applied so that isothermal plateau begins at zero seconds. CH: continuous heating. Error bars are indicated in each graph.

3.2.2. Decomposition of RA during isothermal and cooling stages

As seen in Fig. 4b, no significant variation in the fraction of RA occurs during the isothermal plateau within 550–600°C. However, complete decomposition of RA (RA → ferrite + carbides) happens within the first 600 s of the isothermal plateau at 650°C. The remaining stable RA at the end of the isothermal cycles within 550–600°C transforms into martensite during the cooling stage, as indicated by the vertical arrows in Fig. 4a. The higher the tempering temperature, the higher the M_s temperature, which is indicated in Table 2.

The fraction of tempered martensite can be estimated from the microstructural balance at the end of the isothermal plateau (100% – RA); while the fraction of fresh martensite (M_{fresh}) can be determined as the difference between RA before cooling and RA after cooling. Therefore, the microstructures after tempering consist in a matrix of 80% tempered martensite and increasing fractions of fresh martensite as the tempering temperature increases. A summary of the volume fraction of RA before tempering, right before cooling and after cooling is shown in Table 2, as well as the volume fraction of tempered and fresh martensite, and the M_s temperature. The M_s temperature was experimentally determined by the intersection of the two tangents, and it corresponds to the transformation temperature of the RA at each tempering cycle. After tempering at 650°C, ferrite and carbides (volume fractions not shown in the table) are observed instead of fresh martensite due to the complete isothermal decomposition of RA.

Table 2. Phase quantification of RA, tempered martensite and fresh martensite calculated from full scan measurements. The M_s temperature was retrieved from the cooling curves in Fig. 4 and the error was calculated from the data dispersion

Tempering temperature [°C]	Austenite [%-vol.]			Tempered Martensite [%-vol.]	Fresh Martensite [%-vol.]	M_s [°C]
	As-built	Before cooling	After cooling			
550	24	20	6	80	14	260 ± 16

580	24	20	3	80	17	328 ± 17
600	24	20	2	80	18	347 ± 18
650	20	0	0	80	0	---

3.2.3. Evolution of lattice parameter and FWHM of martensite and RA

Fig. 5 shows the evolution of the lattice parameters of martensite and RA, based on the BCC {200} and FCC {200} peaks, respectively. During heating and cooling, thermal expansions and contractions, respectively, are responsible for the linear behavior in the lattice parameters of martensite (Fig. 5a) and RA (Fig. 5c). Small deviations from linearity, associated to the onset of phase transformations, are observed right before reaching the isothermal stage, especially above 550°C. A clear non-linear lattice parameter reduction for martensite and RA can be noticed during continuous heating, especially between 550 and 743°C, indicating carbon depletion for both phases.

During the isothermal plateau of the tempering cycles, the reduction in the lattice parameters of martensite (Fig. 5b) and RA (Fig. 5d) accelerates as the tempering temperature is increased. For example, the martensite lattice parameter drops to an almost constant value in the first 600 s at 650°C, while complete decomposition of RA simultaneously occurs. However, at 550°C, the reduction of the lattice parameters of both phases is more gradual and continuous, and within 1h of isothermal holding the martensite lattice parameter does not reach the values observed in the 650°C tempering experiment. These net reductions in lattice parameter of both phases can be associated with compositional evolution, i.e., carbon depletion of martensite and RA. Additionally, during cooling from 550–600°C tempering, the points of deviation from linearity of RA, i.e., lattice parameter increment, are consistent with the M_s temperatures, indicated by vertical arrows in Fig. 5c.
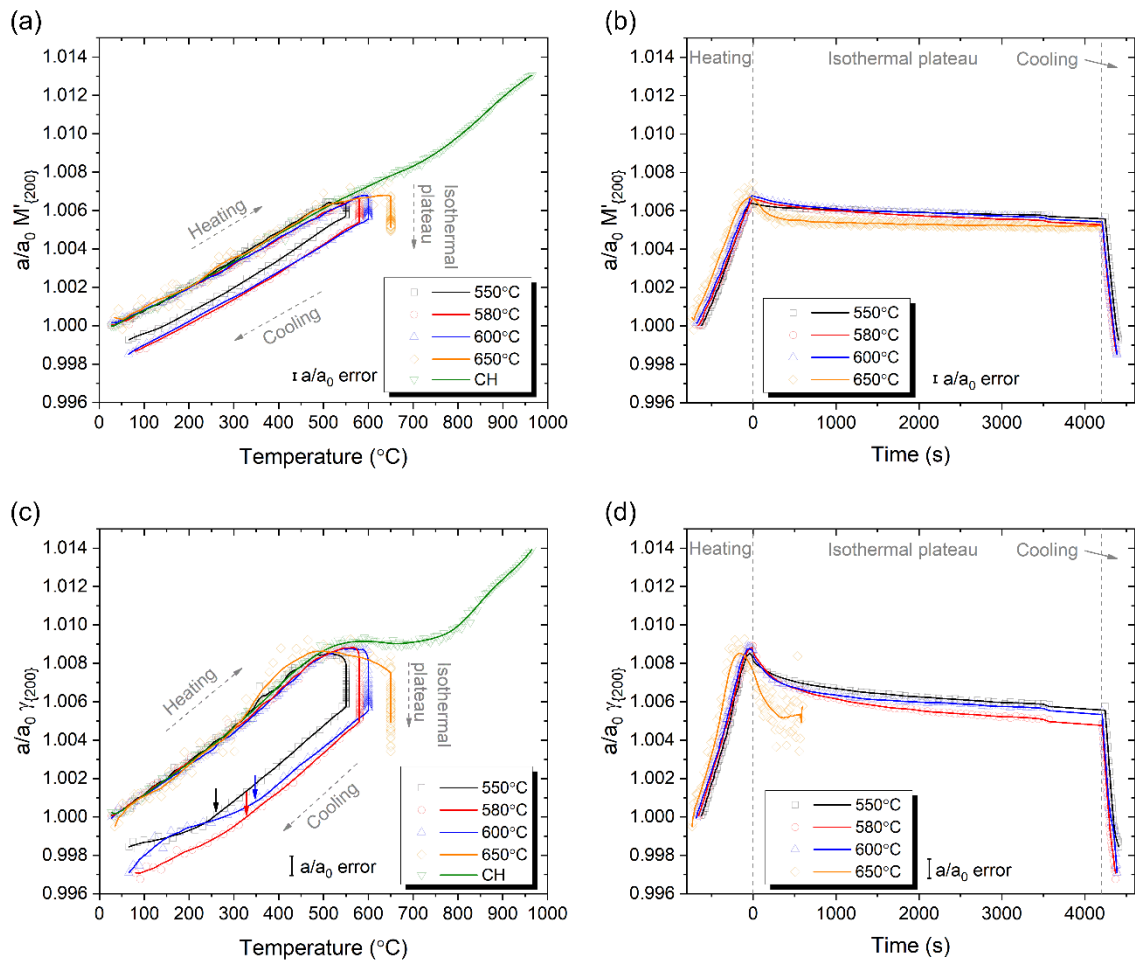
Fig. 5. Lattice parameter evolution retrieved from the {200} peaks of (a-b) martensite/ferrite and (c-d) RA during the tempering cycles of an AISI H13 tool steel in the as-built condition. Temperature-resolved (a, c) and time-resolved (b, d) calculations are provided. Hollow symbols are experimentally retrieved points. Continuous lines were obtained after smoothing the experimental points by a weighted moving average method. Solid symbols correspond to full scan measurements. A time offset in (b) was applied for the isothermal plateau to begin at zero seconds. CH: continuous heating. Error bars are indicated in each graph.

The evolution of the FWHM of the BCC {200} and FCC {200} peaks, during the tempering cycles, is shown in Fig. 6. The FWHM of martensite (Fig. 6a) and RA (Fig. 6c) during the heating stage remain constant until approximately 450°C, followed by a modest reduction before reaching the isothermal temperatures. The CH cycle shows continuous reduction in the FWHM as a function of temperature between 550 and 900°C. Total peak refinements of 70–80%, compared to the normalized value (from 1.0 to 0.3–0.2), are achieved for both phases near 965°C. Similar FWHM values for martensite are

observed at the end of the isothermal stage after tempering at 650°C (Fig. 6b). These reductions in FWHM can be rationalized as the process of effective microstructural softening, via reduction of the dislocation density of both phases through recovery or recrystallization, if the material still stores sufficient energy [1,10,18,32].

During tempering at 550–600°C, more extensive and faster reductions in FWHM of martensite are observed as the tempering temperature increases. However, RA shows little additional reduction in FWHM (Fig. 6d) since most of it occurs during the heating stage. Upon cooling, the FWHM of martensite remains constant until the M_s temperature is reached. Afterwards, peak widening occurs again due to the convolution of fresh martensite (with a high dislocation density) and the tempered martensite matrix (with a reduced dislocation density).

Contrasting, the austenite shows continuous peak widening as soon as the cooling stage initiates, indicating that RA is in a highly unstable condition after tempering. Three phenomena can explain this. First, as the martensitic matrix cools down, it induces higher strain in the soft austenite phase due to different thermal expansion coefficients. Second, when M_s is reached, the expansion associated to martensitic transformation further strains the remaining austenite. The last phenomenon is related to the X-ray diffraction technique itself. As the austenite volume fraction decreases – and thus the RA grain size decreases – due to martensitic transformation, the peaks in X-ray diffraction become less intense and wider, further increasing FWHM.
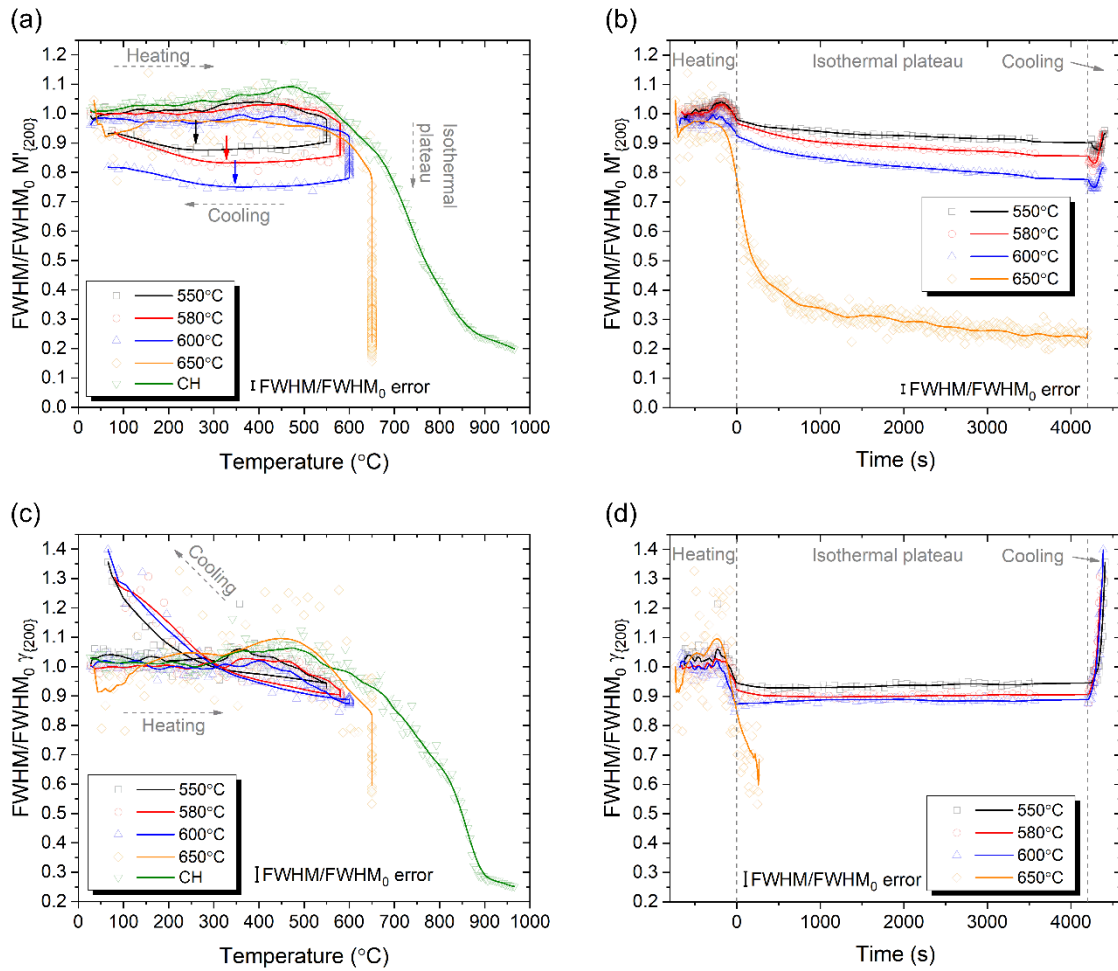
Fig. 6. FWHM evolution retrieved from the {200} peaks of (a-b) martensite/ferrite and (c-d) RA during the tempering cycles of an AISI H13 tool steel in the as-built condition. Temperature-resolved (a, c) and time-resolved (b, d) calculations are provided. Hollow symbols are experimentally retrieved points. Continuous lines were obtained after smoothing the experimental points every 10-points by a weighted moving average method. A time offset in (b) was applied so that isothermal plateau to begin at zero seconds. CH: continuous heating. Error bars are indicated in each graph.

3.3. APT compositional analysis of martensite and RA

3.3.1. Elemental distribution in the as-built condition

Fig. 7 displays 2D concentration profiles of C, Cr, V, Mo, Mn, and Fe relative to the microstructures in the as-built condition (a, b) and after tempering at 550°C (c). The as-built microstructure is characterized by a very heterogeneous distribution of the alloying elements. The upper part of the tip shows a C, Cr, V, Mo, and Mn richer region, here associated to a cell wall in agreement with other previous results in literature [10,11,24,33]. This region is interpreted as a highly segregated RA due to its high C

content (above 3 at.%) and its preferential position at a cell wall. Representative reconstructions of APT tips for the as-built and tempered conditions are shown in Fig. S4 in the Supplementary Material with the C isosurfaces outlining the interface between RA and martensite.

Outside the cell walls, the martensite matrix exhibits an average C concentration below 1 at.%. Within the martensitic structure, other mid-carbon features (average C contents around 1–2 at.%) can be distinguished, for example, by the presence of parallel interfaces, potentially associated to lath interfaces or grain boundaries [17]. For example, Fig. 7b shows a 90°-rotation of the bottom region of Fig. 7a, in which black arrows highlight two C-rich parallel features. These features contain slightly higher concentrations of C, Cr, V, and Mo. Additionally, small globular V aggregates, marked by the black arrow in Fig. 7a, suggest the onset of VC clustering in the as-built microstructure.

3.3.2. *Elemental distribution after tempering at 575°C*

The compositional evolution after tempering at 575°C (Fig. 2c), which produced the maximum secondary hardening, is particularly interesting. The elemental distributions of C, Cr, V, Mo, Mn, and Fe are shown in Fig. 7c. Near the apex of the tip (top region of the 2D concentration profiles) clusters of C, Cr, V, and Mo are visible within the low C tempered martensite. Just below this region, a cluster-free region is also present. The cluster-free M'-(1) and cluster-rich M'-(2) regions might correspond to martensite laths formed at different temperatures [34].

A prior RA region (rich in Cr, V, Mo, and Mn) at a non-solubilized cell wall (Fig. 2c) can also be observed. Interestingly, the C distribution inside this region is heterogeneous. Regions with C concentration above 4 at.% are most likely portions of residual RA (approximately 3%-vol.), while the regions with lower C concentrations are related to fresh martensite, product of RA decomposition. Fewer RA grains are found in the tempered APT tips due to the reduced RA volume fraction after tempering, as indicated in Table 2. Two interfaces near the bottom of the tip (highlighted in the Mn concentration profile) show local spikes of C, Cr, V, Mo, and Mn. These interfaces are assumed to be martensite/RA boundaries [35,36].

Table 3 shows the chemical composition of the RA, M', M_{fresh}, M'-(1) and M'-(2) by positioning ROIs within these regions followed by peak deconvolution analysis. Each region listed in Table 3 is identified in Fig. 7a and c. These compositions were used to estimate the M_s transformation temperature using the extended equation proposed by

Barbier [37]. Although the M_s of RA in the as-built and tempered conditions are above room temperature, RA remained in the evaluated specimens, indicating that the martensite finish temperature (M_f) is still below room temperature.

A much higher M_s temperature is expected for the as-built martensite composition, indicating that transformation potentially takes place at circa 408°C during cooling from L-PBF. In the tempered sample, the compositions of RA and M_{fresh} are very similar except for the C content. As a result, the M_s temperature of M_{fresh} is higher than that of RA, which has a higher C content. The M_s for regions M'-(1) and M'-(2) correspond to the transformation that took place during L-PBF and they are consistent with the values obtained for martensite in the as-built condition and for M_{fresh} in the tempered condition.
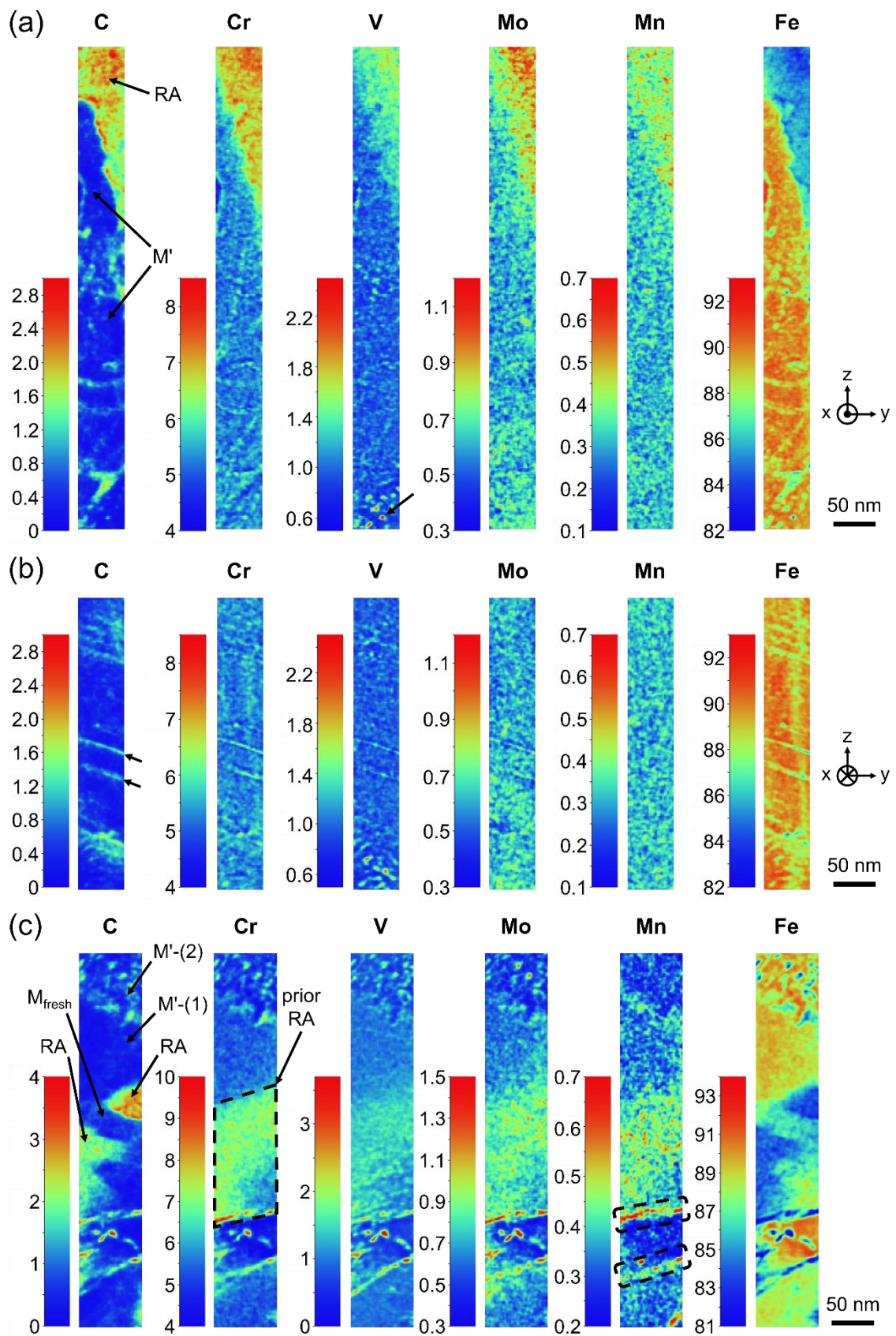
Fig. 7. Atom probe tomography compositional analysis (at.%) presented by 2-D concentration profile heat-maps obtained from: (a-b) two orthogonal rotations of an ROI

in the as-built sample, and (c) sample tempered at 575°C. M': martensite, RA: retained austenite, M_{fresh}: fresh martensite. Notice (b) corresponds to the orthogonal rotation of the bottom region of (a). Concentrations are in at.%. ROI dimensions for the as-built case were 25 x 55 x 570 nm³. ROI dimensions for the tempered condition were 25 x 75 x 440 nm³.

Table 3. Chemical composition (at.%) and M_s temperature of retained austenite (RA) and martensite regions as indicated in Fig. 7. Compositions were calculated after peak deconvolution using ROIs in the as-built and tempered samples.

Sample	ROI	Composition [at.%]							M_s [°C]
		Fe	C	Cr	V	Mo	Mn	Si	
As-built	RA	Bal.	3.71± 0.03	7.16± 0.02	1.44± 0.01	0.87± 0.01	0.42± 0.01	1.98± 0.01	134
	M'	Bal.	0.53± 0.01	5.47± 0.01	0.97± 0.01	0.58± 0.01	0.31± 0.01	2.23± 0.08	408
Tempered 575°C	RA	Bal.	3.91± 0.02	7.46± 0.03	1.45± 0.01	0.88± 0.01	0.45± 0.01	1.97± 0.02	119
	M_{fresh}	Bal.	0.55± 0.02	7.57± 0.03	1.49± 0.01	0.87± 0.02	0.44± 0.01	1.88± 0.04	383
	M'-(1)	Bal.	0.42± 0.01	5.68± 0.01	1.01± 0.01	0.62± 0.01	0.34± 0.01	2.19± 0.10	416
	M'-(2)	Bal.	0.96± 0.01	5.48± 0.01	0.94± 0.01	0.55± 0.01	0.31± 0.01	1.98± 0.10	367

Fig. 8 shows the results of clustering analysis within the martensite matrix using the nearest neighbor distribution method for C, V, Cr, and Mo individually. Carbon clustering is readily present in the as-built condition and is also observed after tempering, as shown in Fig. 8a. The experimental distribution for V, depicted in Fig. 8b, evidences a small deviation from the random distribution in the as-built condition. However, the significant shift toward lower d-pair values in the experimental distribution for the tempered specimens indicates the onset of V clustering in martensite. Both Cr and Mo show negligible clustering in martensite in the as-built and tempered conditions, as shown in Fig. 8c and d, respectively. For the specimens with significant clustering, either carbon clusters in the as-built and tempered conditions and vanadium clusters in the

tempered condition, cluster composition profiles are shown in Fig. S5 in the Supplementary Material. While in the as-built condition the C clusters displayed a slight increase in V and Cr content, in the tempered condition a significant increase in Cr, V, and Mo is observed. The concentration profile of the V clusters in the tempered specimen shows an increased content of C, Cr, and Mo inside the clusters.
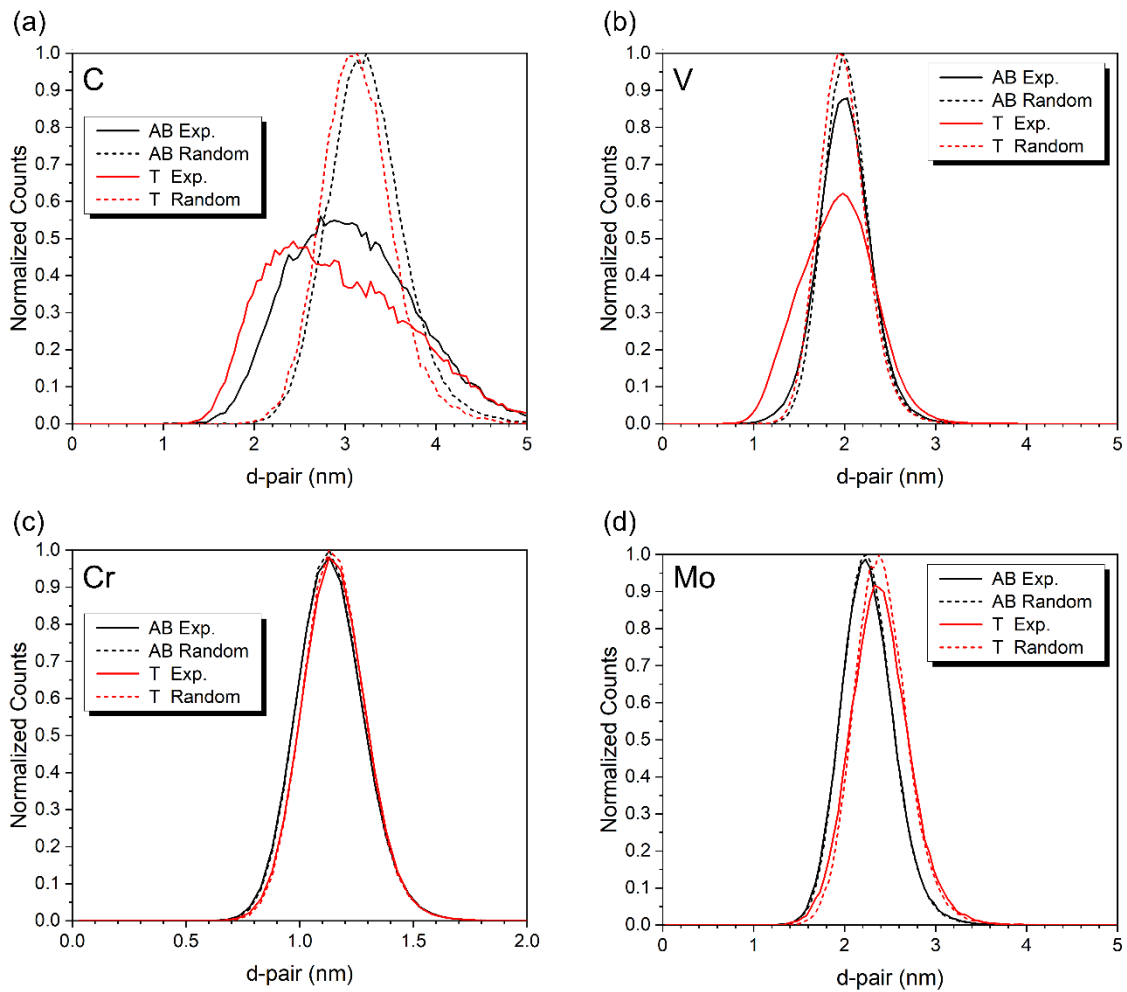

Fig. 8. Nearest neighbor distribution for (a) C, (b) V, (c) Cr, and (d) Mo for representative samples in the as-built (AB) and tempered at 575°C (T) conditions. Experimental distributions shown as continuous lines and random distribution shown in dashed lines. Analyses performed in martensitic regions of the APT tips.

4. Discussion

Our results clarify that the complex network of microsegregations obtained in the as-built condition evolves differently depending on the tempering temperature. Due to microsegregation, local equilibrium conditions need to be considered when investigating

the phase transformations of as-built microstructures. As suggested by Yan et al., two main pathways were identified [22] and are presently correlated to the microsegregated structure. Low temperature transformations (T < 650°C) lead to metastable decomposition of RA, where RA is isothermally stable but transforms into martensite upon cooling, because of RA desaturation during tempering and associated carbide precipitation. High temperature transformations (T ≥ 650°C) imply isothermal ferrite formation, carbide precipitation and coarsening, and almost complete dissolution of microsegregation network. A schematic representation of the microstructural evolution is shown in Fig. 9. To better understand the current findings, we propose to discuss three critical topics: (i) the microsegregated as-built microstructure, and the thermal decomposition (ii) below 650°C, and (iii) above 650°C.
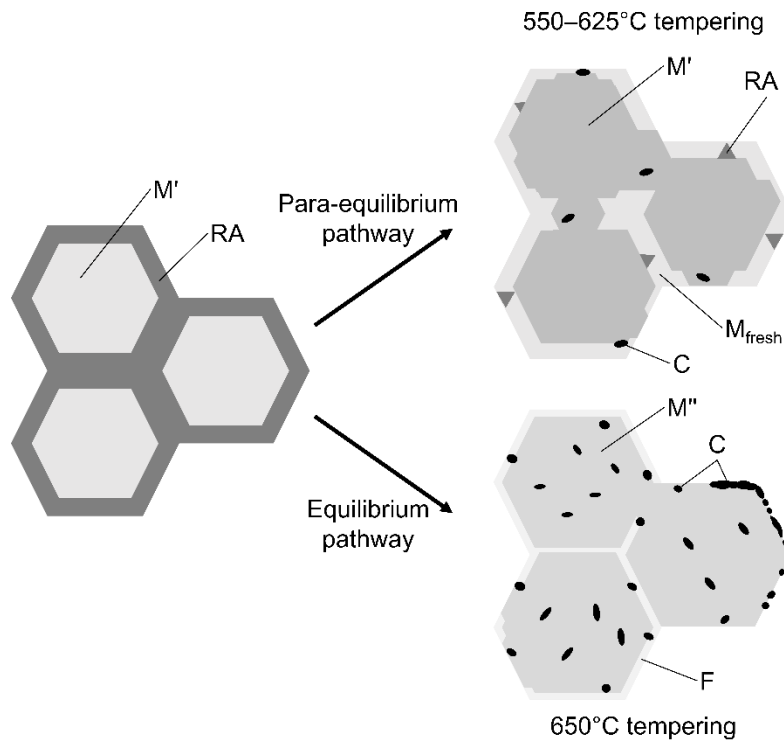
Fig. 9. Pathways for tempering of a highly segregated hot-work tool steel obtained by additive manufacturing with thermally-stable retained austenite. M': martensite, M_{fresh}: fresh martensite transformed from RA after tempering, M'': overtempered martensite, RA: retained austenite, F: ferrite, C: carbide.

4.1. Characterization of the microsegregated microstructure (as-built)

The as-built microstructure is composed of lath martensite (Fig. 3) and circa 24%-vol. RA in a cellular/dendritic solidification structure (Fig. 2a), where RA is mainly at the

24

cell walls (schematically shown in Fig. 9). This microsegregated microstructure is inherent to tool steels processed by L-PBF, laser cladding, and similar rapid solidification processes [8,10,38–40]. APT observations clarify the enrichment of C, Cr, V, and Mo at cell walls where RA is stable. This is consistent with results previously obtained by simulations and semi-quantitative experimental measurements [8,11,41].

The partitioning of elements to RA locally decreases the M_s temperature (Table 3), preventing the formation of a fully martensitic as-built microstructure, as previously stated in the literature [8,25]. The migration of C atoms preferably to lath boundaries even in high dislocation density structures is in agreement with previous literature for other grades of martensitic steels [17,42]. Fig. 10 shows the equilibrium volume fraction of ferrite and austenite as a function of temperature. These thermodynamic calculations are presented for experimentally observed compositions (obtained from APT local analyses) at (i) as-built cell walls (RA), (ii) as-built cell cores (martensite), (iii) tempered cell walls (M_{fresh}). These results are also compared to the nominal composition (solubilized state). The microsegregated microstructure at the cell walls has a complex composition, containing both austenite stabilizing (C) and ferrite stabilizing elements (Cr, Mo). However, the synergic effect of such complex segregation results in a lower A_{e1} temperature than the solubilized state. Whereas the cell core and the decomposed cell wall (M_{fresh}) both show higher A_{e1} temperatures relative to the nominal composition. This confirms that microsegregation at cell walls is the cause of RA stabilizing. Carbon presents a particularly strong effect in the stabilization of RA. This is especially clarified by comparing the A_{e1} temperatures of the as-built and tempered (M_{fresh}) cell walls in Fig. 10, where the main difference is the strong carbon depletion of the latter.
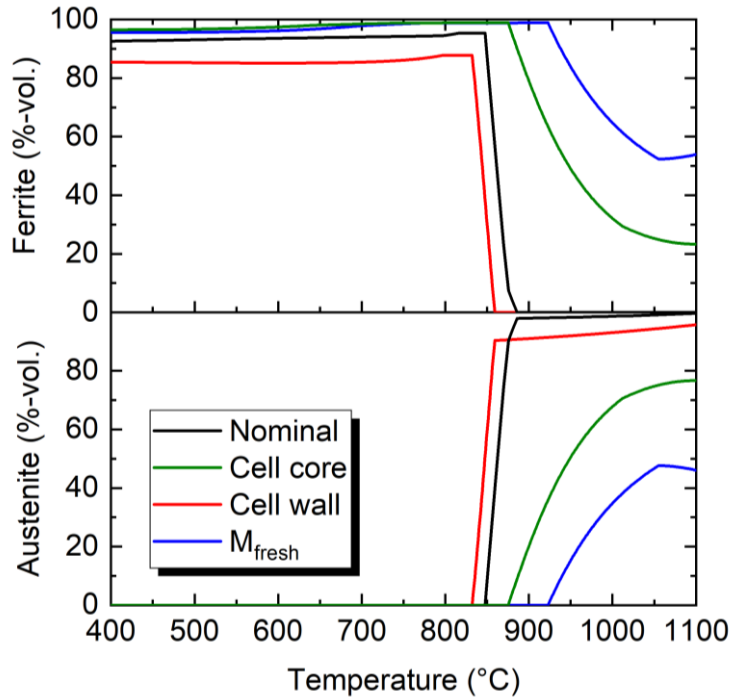
Fig. 10. Equilibrium volume fractions of ferrite and austenite calculated using ThermoCalc software and the TCFE9 database. The simulated cell core, cell wall and M_{fresh} cases are based on the measured compositions using APT local compositional analysis (Table 3).

4.2. The equilibrium pathway: isothermal decomposition of RA into ferrite and carbides

At 650°C tempering, RA fully decomposes within 600 s in the isothermal plateau, as shown by the austenite fraction in Fig. 4b. The decomposition of RA at 650°C is consistent with CCT and TTT diagrams reported in the literature, but it occurs at shorter times than in the wrought counterparts [8,20]. Simultaneously, the lattice parameters and FWHM of austenite and martensite sharply decrease in the beginning of the isothermal plateau. The martensitic lattice parameter reaches a steady value after 600 s, which suggests that martensite is no longer supersaturated in C. The reduction of the martensitic (BCC peaks) FWHM can be explained by two concurrent phenomena: the overtempering of martensite, and the transformation of RA into ferrite, which has a lower dislocation density than martensite. Thus, as the RA transforms into ferrite, FWHM has the convoluted effects of the low-dislocation-density ferrite and the high-dislocation-density martensite. Simultaneously, overtempering of martensite is responsible for stress relaxation, and dislocation rearrangement [27,43], also promoting a reduction of FWHM as the martensite laths coarsen. Both the transformation of RA into ferrite and the

26

overtempering of martensite are accompanied by the precipitation and coarsening of carbides. The resultant microstructure is characterized by ferrite (transformed from RA), and coarsened lath martensite (due to martensite overtempering) and carbides, as observed by SEM in Fig. 2f. Similar microstructures were also reported in L-PBF samples tempered at 650°C for 2h [44] and 5h [45]. These phenomena contribute to the hardness decrease at 650°C tempering. The complete decomposition of RA is accompanied by the dissolution of the solidification structure [8,32], which contributes to the decrease in hardness relative to the other tempered specimens, since the cell walls limit dislocation movement by a dislocation trapping and retention mechanism [22,46,47]. As a result, the hardness of the samples tempered at 650°C was the lowest among the analyzed samples. The 650°C tempering represents the microstructural evolution of the as-built microstructure toward the equilibrium condition.

4.3. The para-equilibrium pathway: isothermal RA stability with martensitic transformation upon cooling

It has been suggested that during tempering of additively manufactured tool steels, RA decomposition and secondary carbide precipitation from martensite occur simultaneously at 600°C [10]. Our direct observations via HTXRD show that during tempering within 550–600°C, RA remains stable during the isothermal plateau and undergoes martensitic transformation upon cooling, as suggested in [22,23,25,27,44]. However, it should be noted that both substructural (FWHM) and compositional (lattice parameter) evolution can take place isothermally. The substructural evolution can be interpreted as the degree of recovery (dislocation annihilation); while the compositional evolution is associated to carbon mobility.

Regarding substructural evolution, Deirmina et al. analyzed a sintered AISI H13 and suggested volumetric recovery starting at 400°C [48]. Nanesa et al. indicated that volumetric recovery occurred at tempering temperatures between 250–500°C, but also stated that the temperature interval can vary with chemical composition [49]. Our phase-specific analysis indicate that recovery occurs in both RA and the martensitic matrix, especially above 500°C, as observed by the onset of FWHM reduction in both phases (Fig. 6a and c). Upon cooling, the FWHM of RA strongly increases, highlighting that this metastable isothermal condition is strongly dependent on temperature.

Simultaneously, the RA lattice parameter reduction in the isothermal plateau (Fig. 5c) suggests a decrease in the content of alloying elements dissolved in RA, as predicted by the relationship between lattice parameter and chemical composition [50]. Our APT

observations in Table 3 show that the decomposed RA (namely M_{fresh}) shows a similar composition relative to the as-built RA, except for carbon depletion. This result indicates that diffusion of substitutional alloying elements is negligible, thus lattice parameter obtained by HTXRD data can be correlated to carbon content. As substitutional alloying elements are assumed to have negligible mobility, para-equilibrium was the term employed to describe such pathway. However, no assertions are made regarding the chemical potential of the elements in RA and martensite. It can be stated that C depletion in RA during the isothermal plateau is responsible for locally increasing the M_s temperature [13], thus leading to martensitic transformation upon cooling. The C depletion in RA due to carbide precipitation during tempering is a known mechanism for promoting martensitic transformation in wrought tool steels [14].

A significant increase in hardness is expected due to RA transformation into fresh martensite. However, hardness depends on the complex interaction between martensitic transformation, secondary hardening, and prior martensite tempering. Despite the higher fraction of fresh martensite after tempering at 600°C (Table 2), the final Vickers hardness is lower than that of samples tempered at 550 or 575°C. During tempering, carbide precipitation, as well as nano-sized C and V clustering occurs (Fig. 8). This leads to a strong secondary hardening effect, especially at 575°C, most likely due to dislocation pinning by the Orowan mechanism. Carbon clustering has been observed in martensitic steels due to autotempering [16,51]. Our data shows C clustering in the as-built condition, followed by additional strengthening of C and V clustering tendencies after tempering at 575°C. The detected C and V clusters also show enrichment in Cr and Mo, which suggests that these nano-sized regions are related to the onset of nucleation of other complex carbides. Besides V-rich MC, the most common carbides in AISI H13 tool steel are V-rich M_8C_7, Cr-rich $M_{23}C_6$ and M_7C_3, and Mo-rich M_6C and M_2C [52,53]. Detailed information regarding cluster compositional analysis is shown in the Supplementary Material (Fig. S5). As clusters and carbides form, alloying elements are consumed from the supersaturated martensitic matrix, reducing the lattice parameter. At higher tempering temperatures (600 and 625°C), martensite laths and carbides slightly coarsen, martensite supersaturation further reduces, and dislocation density declines, leading to a decrease in hardness [27,44].

A large fraction of RA remains stable during continuous heating, even above 650°C. Between 550 and 743°C, the thermal expansion of the austenitic lattice parameter (Fig. 5c) is outweighed by the compositional evolution, i.e., C depletion. Above 743°C, the volume fraction of austenite slightly decreases, but not completely. This indicates the important role of microsegregation on the generation of a metastable

transition state, which leads to a sluggish dissolution of RA and to delayed nucleation of ferrite.

5. Conclusions

The phase transformation kinetics associated with the decomposition of the cell-like microsegregated microstructure of an additively manufactured AISI H13 tool steel is investigated in this work. Time- and temperature-resolved quantification of retained austenite (RA) was obtained during *in-situ* tempering cycles using synchrotron X-ray diffraction. The RA decomposition products were characterized via scanning electron microscopy and atom probe tomography. Multi-modal microstructural analysis clarified that the cellular/dendritic solidification structure retains 20–26%-vol. of RA due to microsegregation of C, Cr, V, and Mo. *In-situ* characterization allowed us to separate the microstructural evolution of this microsegregated microstructure into two decomposition paths: para-equilibrium (T < 650°C) and equilibrium (T ≥ 650°C).

Throughout the para-equilibrium pathway (T < 650°C), the fraction of RA remains mostly unchanged at high temperature, but undergoes martensitic transformation during cooling due to C depletion induced by secondary carbides precipitation. Yet, a residual presence of RA (2–6%-vol.) remains stable at room temperature after tempering for 1h. No significant dissolution of the microsegregation network is observed during low temperature tempering (550–575°C). Secondary hardening occurs due to incipient carbide precipitation and nanometric clustering of C and V. C clusters, already found in the as-built condition due to autotempering, became enriched with Cr, V, and Mo after tempering. In the higher tempering temperature range (600–625°C), the solidification structure partially dissolves, and hardness decreases due to carbide coarsening and martensite recovery.

The equilibrium pathway (T ≥ 650°C) allows direct high temperature decomposition of RA into ferrite and coarse carbides within the first 600 s of the isothermal soaking at 650°C. Temperature-assisted enhanced diffusivity leads to an overtempered microstructure, where the coarsening of martensite laths, coalescence of carbides, reduction of the dislocation density, and dissolution of the microsegregated cell walls promote softening.

These results are useful for the design of novel heat treatment routes that can be more appropriate for microsegregated microstructures. For example, fast single-step tempering cycles (at least 10 minutes at 650°C) will provide soft and overtempered martensite with complete dissolution of RA. Contrasting, low temperature tempering (1h

at 575°C) will produce secondary hardened microstructures containing large quantities of fresh martensite. This offers the potential for custom microstructural design for high toughness or high wear resistance applications, respectively. As it is usual for tool steels, multiple tempering cycles are necessary, especially to temper any fresh martensite. Thus, subsequent tempering cycles need to be assessed for industrial applications.

Acknowledgements

References

[1]   G. Roberts, G. Krauss, R. Kennedy, Tool Steels, 5th Editio, ASM International, 1998. https://doi.org/10.1361/toos1998p001.

[2]   R. Shivpuri, Dies and Die Materials for Hot Forging, in: Metalwork. Bulk Form., ASM International, 2005: pp. 47–61. https://doi.org/10.31399/asm.hb.v14a.a0003975.

[3]   R. Hölker, M. Haase, N. Ben Khalifa, A.E. Tekkaya, Hot Extrusion Dies with Conformal Cooling Channels Produced by Additive Manufacturing, Mater. Today Proc. 2 (2015) 4838–4846. https://doi.org/10.1016/j.matpr.2015.10.028.

[4]   M. Mazur, P. Brincat, M. Leary, M. Brandt, Numerical and experimental evaluation of a conformally cooled H13 steel injection mould manufactured with selective laser melting, Int. J. Adv. Manuf. Technol. 93 (2017) 881–900. https://doi.org/10.1007/s00170-017-0426-7.

[5]   N.P. Karapatis, J.P.S. van Griethuysen, R. Glardon, Direct rapid tooling: a review of current research, Rapid Prototyp. J. 4 (1998) 77–89. https://doi.org/10.1108/13552549810210248.

[6]   M. Mazur, M. Leary, M. McMillan, J. Elambasseril, M. Brandt, SLM additive manufacture of H13 tool steel with conformal cooling and structural lattices, Rapid Prototyp. J. 22 (2016) 504–518. https://doi.org/10.1108/RPJ-06-2014-0075.

[7]   C. Tan, D. Wang, W. Ma, Y. Chen, S. Chen, Y. Yang, K. Zhou, Design and additive manufacturing of novel conformal cooling molds, Mater. Des. 196 (2020) 109147. https://doi.org/10.1016/j.matdes.2020.109147.

[8]   J. Krell, A. Röttger, K. Geenen, W. Theisen, General investigations on processing tool steel X40CrMoV5-1 with selective laser melting, J. Mater. Process. Technol. 255 (2018) 679–688. https://doi.org/10.1016/j.jmatprotec.2018.01.012.

[9]   M.J. Holzweissig, A. Taube, F. Brenne, M. Schaper, T. Niendorf, Microstructural Characterization and Mechanical Performance of Hot Work Tool Steel Processed by Selective Laser Melting, Metall. Mater. Trans. B. 46 (2015) 545–549. https://doi.org/10.1007/s11663-014-0267-9.

[10]   F. Deirmina, N. Peghini, B. AlMangour, D. Grzesiak, M. Pellizzari, Heat treatment and properties of a hot work tool steel fabricated by additive manufacturing, Mater. Sci. Eng. A. 753 (2019) 109–121. https://doi.org/10.1016/j.msea.2019.03.027.

[11]   E.B. Fonseca, A.H.G. Gabriel, L.C. Araújo, P.L.L. Santos, K.N. Campo, E.S.N. Lopes, Assessment of laser power and scan speed influence on microstructural features and consolidation of AISI H13 tool steel processed by additive manufacturing, Addit. Manuf. 34 (2020) 101250. https://doi.org/10.1016/j.addma.2020.101250.

[12]   M. Pérez, F.J. Belzunce, The effect of deep cryogenic treatments on the mechanical properties of an AISI H13 steel, Mater. Sci. Eng. A. 624 (2015) 32–40. https://doi.org/10.1016/j.msea.2014.11.051.

[13]   C. Lerchbacher, S. Zinner, H. Leitner, Direct or indirect: Influence of type of retained austenite decomposition during tempering on the toughness of a hot-work tool steel, Mater. Sci. Eng. A. 564 (2013) 163–168.

https://doi.org/10.1016/j.msea.2012.11.105.

[14] G.E. Totten, ed., Steel Heat Treatment: Metallurgy and Technologies, 2nd editio, Taylor & Francis, 2006.

[15] A. Çiçek, F. Kara, T. Kıvak, E. Ekici, İ. Uygur, Effects of Deep Cryogenic Treatment on the Wear Resistance and Mechanical Properties of AISI H13 Hot-Work Tool Steel, J. Mater. Eng. Perform. 24 (2015) 4431–4439. https://doi.org/10.1007/s11665-015-1712-x.

[16] L. Morsdorf, E. Emelina, B. Gault, M. Herbig, C.C. Tasan, Carbon redistribution in quenched and tempered lath martensite, Acta Mater. 205 (2021) 116521. https://doi.org/10.1016/j.actamat.2020.116521.

[17] B. Hutchinson, J. Hagström, O. Karlsson, D. Lindell, M. Tornberg, F. Lindberg, M. Thuvander, Microstructures and hardness of as-quenched martensites (0.1–0.5%C), Acta Mater. 59 (2011) 5845–5858. https://doi.org/10.1016/j.actamat.2011.05.061.

[18] M. Hunkel, J. Dong, J. Epp, D. Kaiser, S. Dietrich, V. Schulze, A. Rajaei, B. Hallstedt, C. Broeckmann, Comparative Study of the Tempering Behavior of Different Martensitic Steels by Means of In-Situ Diffractometry and Dilatometry, Materials (Basel). 13 (2020) 5058. https://doi.org/10.3390/ma13225058.

[19] M. Kulakov, W.J. Poole, M. Militzer, The effect of the initial microstructure on recrystallization and austenite formation in a DP600 steel, Metall. Mater. Trans. A Phys. Metall. Mater. Sci. 44 (2013) 3564–3576. https://doi.org/10.1007/s11661-013-1721-z.

[20] R.A. Mesquita, R. Schneider, C.S. Gonçalves, Heat Treating of Hot-Work Tool Steels, in: Heat Treat. Irons Steels, ASM International, 2014: pp. 336–346. https://doi.org/10.31399/asm.hb.v04d.a0005974.

[21] M. Åsberg, G. Fredriksson, S. Hatami, W. Fredriksson, P. Krakhmalev, Influence of post treatment on microstructure, porosity and mechanical properties of additive manufactured H13 tool steel, Mater. Sci. Eng. A. 742 (2019) 584–589. https://doi.org/10.1016/j.msea.2018.08.046.

[22] J. Yan, H. Song, Y. Dong, W.M. Quach, M. Yan, High strength (~2000 MPa) or highly ductile (~11%) additively manufactured H13 by tempering at different conditions, Mater. Sci. Eng. A. 773 (2020) 138845. https://doi.org/10.1016/j.msea.2019.138845.

[23] D. Junker, O. Hentschel, M. Schmidt, M. Merklein, Investigation of Heat Treatment

Strategies for Additively-Manufactured Tools of X37CrMoV5-1, Metals (Basel). 8 (2018) 854. https://doi.org/10.3390/met8100854.

[24] M. Pellizzari, S. Furlani, F. Deirmina, R. Siriki, B. AlMangour, D. Grzesiak, Fracture Toughness of a Hot Work Tool Steel Fabricated by Laser-Powder Bed Fusion Additive Manufacturing, Steel Res. Int. 91 (2020) 1–7. https://doi.org/10.1002/srin.201900449.

[25] S. Amirabdollahian, F. Deirmina, M. Pellizzari, P. Bosetti, A. Molinari, Tempering behavior of a direct laser deposited hot work tool steel: Influence of quenching on secondary hardening and microstructure, Mater. Sci. Eng. A. 814 (2021) 141126. https://doi.org/10.1016/j.msea.2021.141126.

[26] R. Mertens, B. Vrancken, N. Holmstock, Y. Kinds, J.P. Kruth, J. Van Humbeeck, Influence of powder bed preheating on microstructure and mechanical properties of H13 tool steel SLM parts, Phys. Procedia. 83 (2016) 882–890. https://doi.org/10.1016/j.phpro.2016.08.092.

[27] C.J. Chen, K. Yan, L. Qin, M. Zhang, X. Wang, T. Zou, Z. Hu, Effect of Heat Treatment on Microstructure and Mechanical Properties of Laser Additively Manufactured AISI H13 Tool Steel, J. Mater. Eng. Perform. 26 (2017) 5577–5589. https://doi.org/10.1007/s11665-017-2992-0.

[28] B.D. Cullity, Elements of X-ray diffraction, 1978.

[29] J.D. Escobar, G.A. Faria, L. Wu, J.P. Oliveira, P.R. Mei, A.J. Ramirez, Austenite reversion kinetics and stability during tempering of a Ti-stabilized supermartensitic stainless steel: Correlative in situ synchrotron x-ray diffraction and dilatometry, Acta Mater. 138 (2017) 92–99. https://doi.org/10.1016/j.actamat.2017.07.036.

[30] G.A. Faria, Exploring Metallic Materials Behavior Through In Situ Crystallographic Studies, University of Campinas, 2014. http://repositorio.unicamp.br/jspui/handle/REPOSIP/265849.

[31] J. Lee, Y. Jeong, D. Shim, E. Lee, Microstructural evolution and martensitic transformation in FeCrV alloy fabricated via additive manufacturing, Mater. Sci. Eng. A. 809 (2021) 140943. https://doi.org/10.1016/j.msea.2021.140943.

[32] M. Wang, W. Li, Y. Wu, S. Li, C. Cai, S. Wen, Q. Wei, Y. Shi, F. Ye, Z. Chen, High-Temperature Properties and Microstructural Stability of the AISI H13 Hot-Work Tool Steel Processed by Selective Laser Melting, Metall. Mater. Trans. B. 50 (2019) 531–542. https://doi.org/10.1007/s11663-018-1442-1.

[33] J. Mazumder, J. Choi, K. Nagarathnam, J. Koch, D. Hetzner, The direct metal

deposition of H13 tool steel for 3-D components, JOM. 49 (1997) 55–60. https://doi.org/10.1007/BF02914687.

[34]   C. Lerchbacher, S. Zinner, H. Leitner, Atom probe study of the carbon distribution in a hardened martensitic hot-work tool steel X38CrMoV5-1, Micron. 43 (2012) 818–826. https://doi.org/10.1016/j.micron.2012.02.005.

[35]   A. Devaraj, Z. Xu, F. Abu-Farha, X. Sun, L.G. Hector, Nanoscale Solute Partitioning and Carbide Precipitation in a Multiphase TRIP Steel Analyzed by Atom Probe Tomography, JOM. 70 (2018) 1752–1757. https://doi.org/10.1007/s11837-018-2974-1.

[36]   J.D. Escobar, J.D. Poplawsky, G.A. Faria, J. Rodriguez, J.P. Oliveira, C.A.F. Salvador, P.R. Mei, S.S. Babu, A.J. Ramirez, Compositional analysis on the reverted austenite and tempered martensite in a Ti-stabilized supermartensitic stainless steel: Segregation, partitioning and carbide precipitation, Mater. Des. 140 (2018) 95–105. https://doi.org/10.1016/j.matdes.2017.11.055.

[37]   D. Barbier, Extension of the Martensite Transformation Temperature Relation to Larger Alloying Elements and Contents, Adv. Eng. Mater. 16 (2014) 122–127. https://doi.org/10.1002/adem.201300116.

[38]   R. Vilar, R. Colaço, A. Almeida, Laser surface treatment of tool steels, Opt. Quantum Electron. 27 (1995) 1273–1289.

[39]   P. Kattire, S. Paul, R. Singh, W. Yan, Experimental characterization of laser cladding of CPM 9V on H13 tool steel for die repair applications, J. Manuf. Process. 20 (2015) 492–499. https://doi.org/10.1016/j.jmapro.2015.06.018.

[40]   G. Telasang, J. Dutta Majumdar, G. Padmanabham, M. Tak, I. Manna, Effect of laser parameters on microstructure and hardness of laser clad and tempered AISI H13 tool steel, Surf. Coatings Technol. 258 (2014) 1108–1118. https://doi.org/10.1016/j.surfcoat.2014.07.023.

[41]   F. Deirmina, B. AlMangour, D. Grzesiak, M. Pellizzari, H13–partially stabilized zirconia nanocomposites fabricated by high-energy mechanical milling and selective laser melting, Mater. Des. 146 (2018) 286–297. https://doi.org/10.1016/j.matdes.2018.03.017.

[42]   S. Aoued, F. Danoix, S.Y.P. Allain, S. Gaudez, G. Geandier, J.-C. Hell, M. Soler, M. Gouné, Microstructure Evolution and Competitive Reactions during Quenching and Partitioning of a Model Fe–C–Mn–Si Alloy, Metals (Basel). 10 (2020) 137. https://doi.org/10.3390/met10010137.

[43] M. Zhang, C. Li, Q. Gao, J. Fang, T.L. Wu, K.H. Wang, The effect of heat treatment on microstructure and properties of laser-deposited TiC reinforced H13 steel matrix composites, Optik (Stuttg). 206 (2020) 164286. https://doi.org/10.1016/j.ijleo.2020.164286.

[44] M. Katancik, S. Mirzababaei, M. Ghayoor, S. Pasebani, Selective laser melting and tempering of H13 tool steel for rapid tooling applications, J. Alloys Compd. 849 (2020) 156319. https://doi.org/10.1016/j.jallcom.2020.156319.

[45] A.M. Vilardell, S.B. Hosseini, M. Åsberg, A. Dahl-Jendelin, P. Krakhmalev, C. Oikonomou, S. Hatami, Evaluation of post-treatments of novel hot-work tool steel manufactured by laser powder bed fusion for aluminum die casting applications, Mater. Sci. Eng. A. 800 (2021) 140305. https://doi.org/10.1016/j.msea.2020.140305.

[46] Y.M. Wang, T. Voisin, J.T. McKeown, J. Ye, N.P. Calta, Z. Li, Z. Zeng, Y. Zhang, W. Chen, T.T. Roehling, R.T. Ott, M.K. Santala, P.J. Depond, M.J. Matthews, A. V. Hamza, T. Zhu, Additively manufactured hierarchical stainless steels with high strength and ductility, Nat. Mater. 17 (2018) 63–71. https://doi.org/10.1038/nmat5021.

[47] Y. Zhong, L. Liu, S. Wikman, D. Cui, Z. Shen, Intragranular cellular segregation network structure strengthening 316L stainless steel prepared by selective laser melting, J. Nucl. Mater. 470 (2016) 170–178. https://doi.org/10.1016/j.jnucmat.2015.12.034.

[48] F. Deirmina, M. Pellizzari, Strengthening mechanisms in an ultrafine grained powder metallurgical hot work tool steel produced by high energy mechanical milling and spark plasma sintering, Mater. Sci. Eng. A. 743 (2019) 349–360. https://doi.org/10.1016/j.msea.2018.11.093.

[49] H.G. Nanesa, H. Touazine, M. Jahazi, Influence of cryogenic process parameters on microstructure and hardness evolution of AISI D2 tool steel, Int. J. Adv. Manuf. Technol. 85 (2016) 881–890. https://doi.org/10.1007/s00170-015-7980-7.

[50] S.S. Babu, E.D. Specht, S.A. David, E. Karapetrova, P. Zschack, M. Peet, H.K.D.H. Bhadeshia, In-Situ Observations of Lattice Parameter Fluctuations in Austenite and Transformation to Bainite, Metall. Mater. Trans. A. 36 (2005) 3281–3289. https://doi.org/10.1007/s11661-005-0002-x.

[51] C. Lerchbacher, S. Zinner, H. Leitner, Retained Austenite Decomposition and Carbide Formation During Tempering a Hot-Work Tool Steel X38CrMoV5-1

Studied by Dilatometry and Atom Probe Tomography, Metall. Mater. Trans. A. 43 (2012) 4989–4998. https://doi.org/10.1007/s11661-012-1358-3.

[52]   J. Lee, J. Choe, J. Park, J.-H. Yu, S. Kim, I.D. Jung, H. Sung, Microstructural effects on the tensile and fracture behavior of selective laser melted H13 tool steel under varying conditions, Mater. Charact. 155 (2019) 109817. https://doi.org/10.1016/j.matchar.2019.109817.

[53]   N. Angang, G. Hanjie, C. Xichun, W. Mingbo, Precipitation Behaviors and Strengthening of Carbides in H13 Steel during Annealing, Mater. Trans. 56 (2015) 581–586. https://doi.org/10.2320/matertrans.M2014452.

Supplementary Material
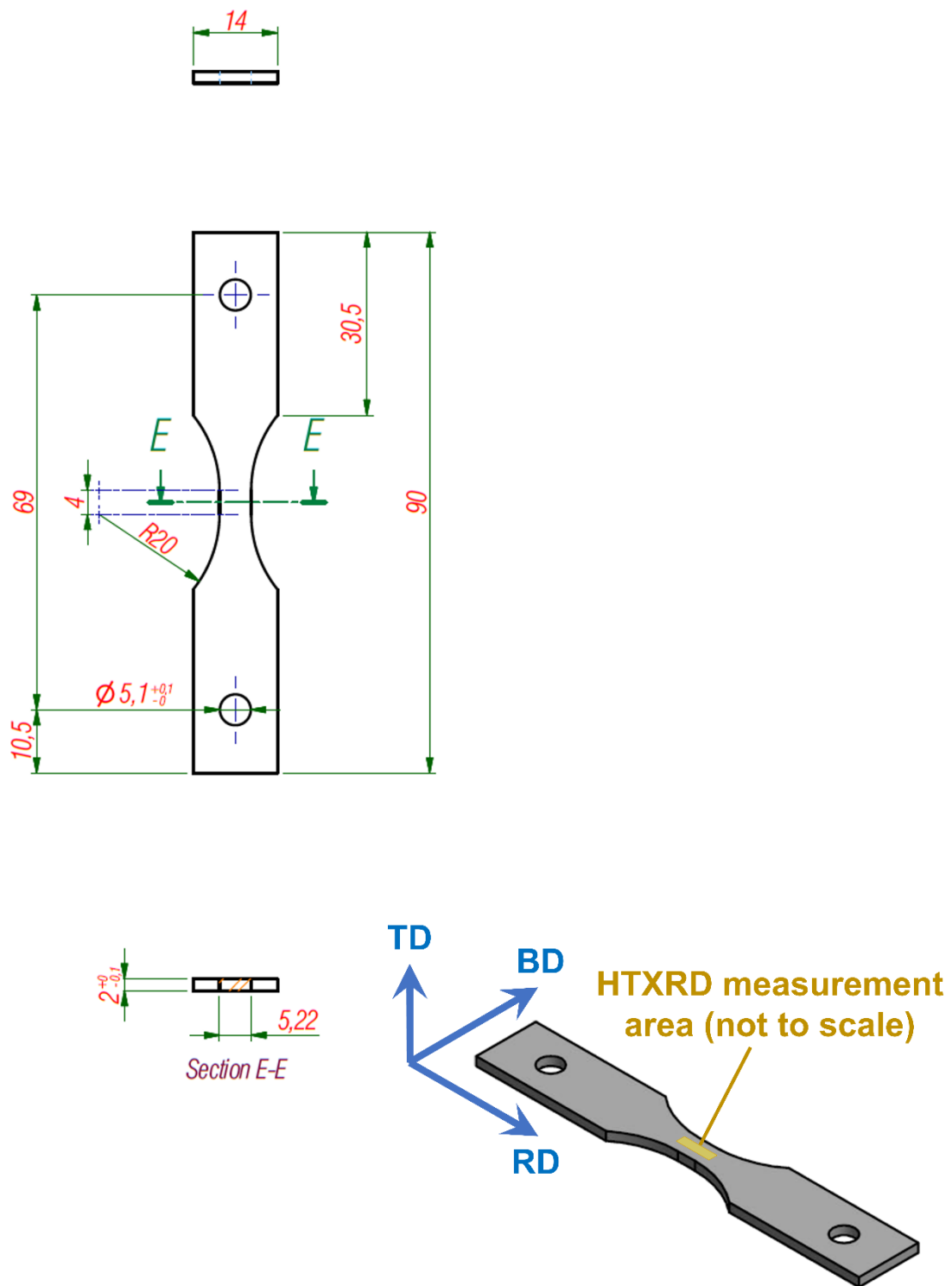
Fig. S1. Bow tie specimens produced by L-PBF and used in high-temperature *in-situ* synchrotron X-ray diffraction (HTXRD) experiments. BD: build direction; RD: recoater direction; TD: transverse direction. Dimensions in mm.
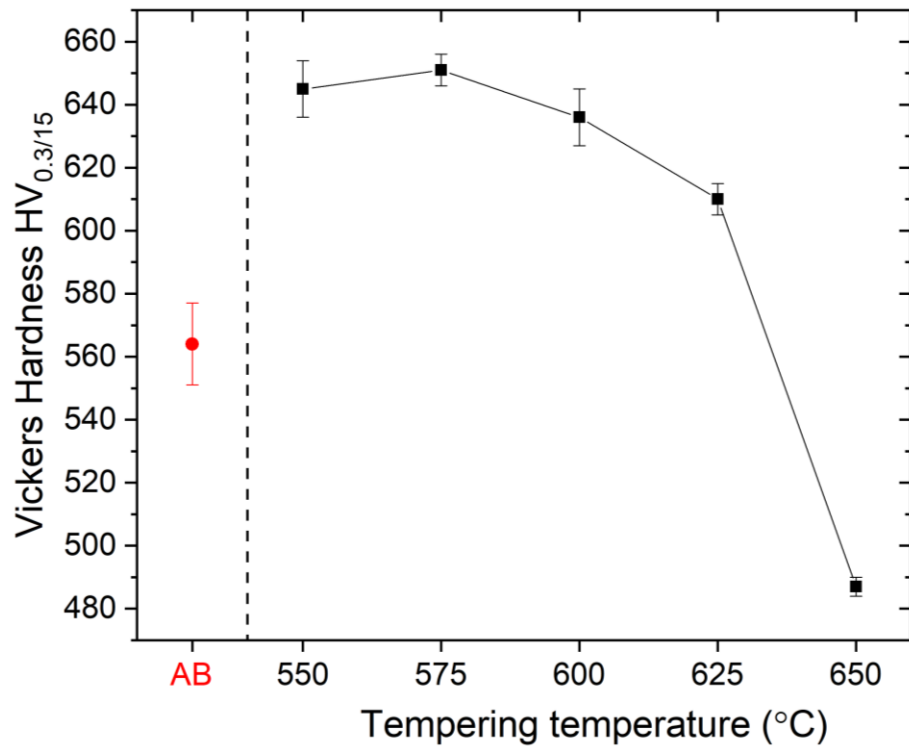
Fig. S2. Tempering curve of the AISI H13 tool steel produced by L-PBF. Heat treatments were performed in an electric resistance furnace for 1h. AB: as-built.
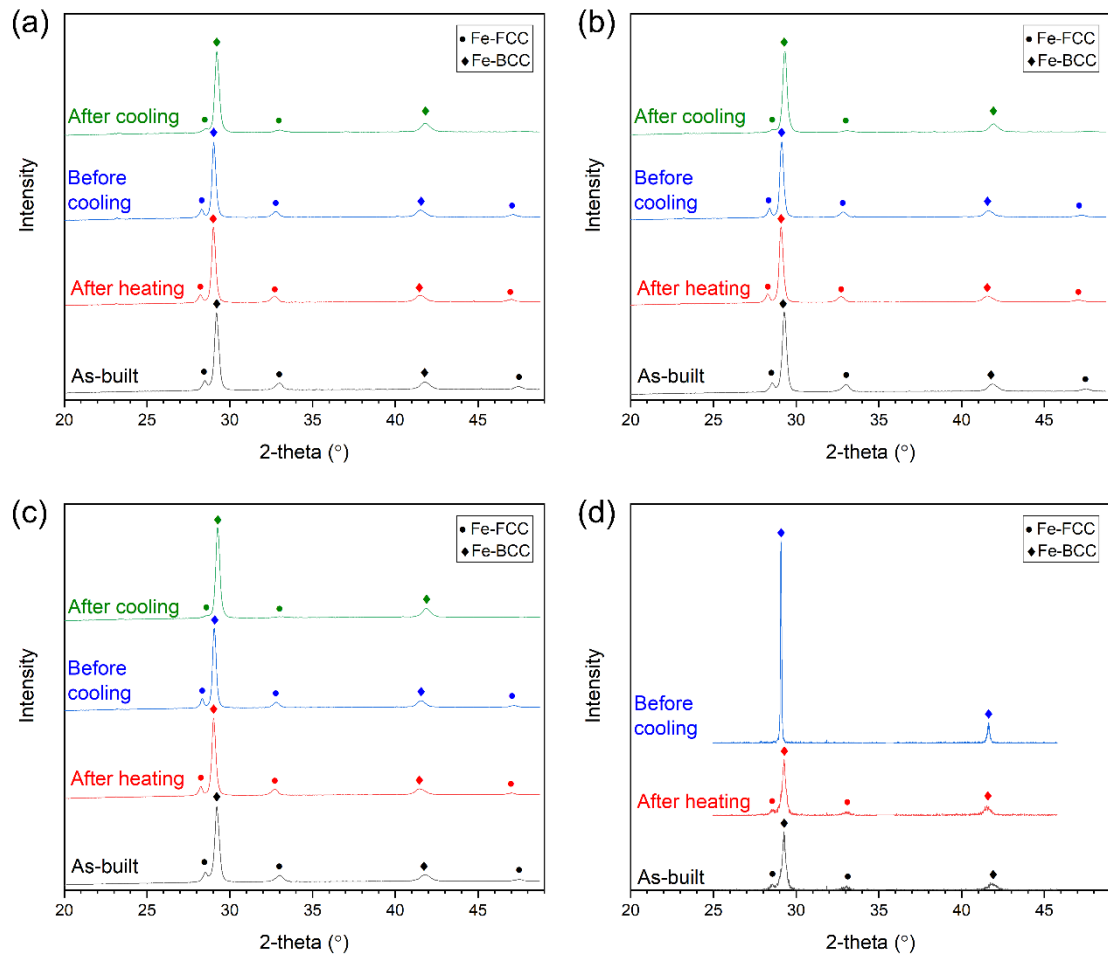
Fig. S3. Representative diffractograms obtained in HTXRD experiments for the tempering heat treatments at (a) 550, (b) 580, (c) 600, and (d) 650°C.
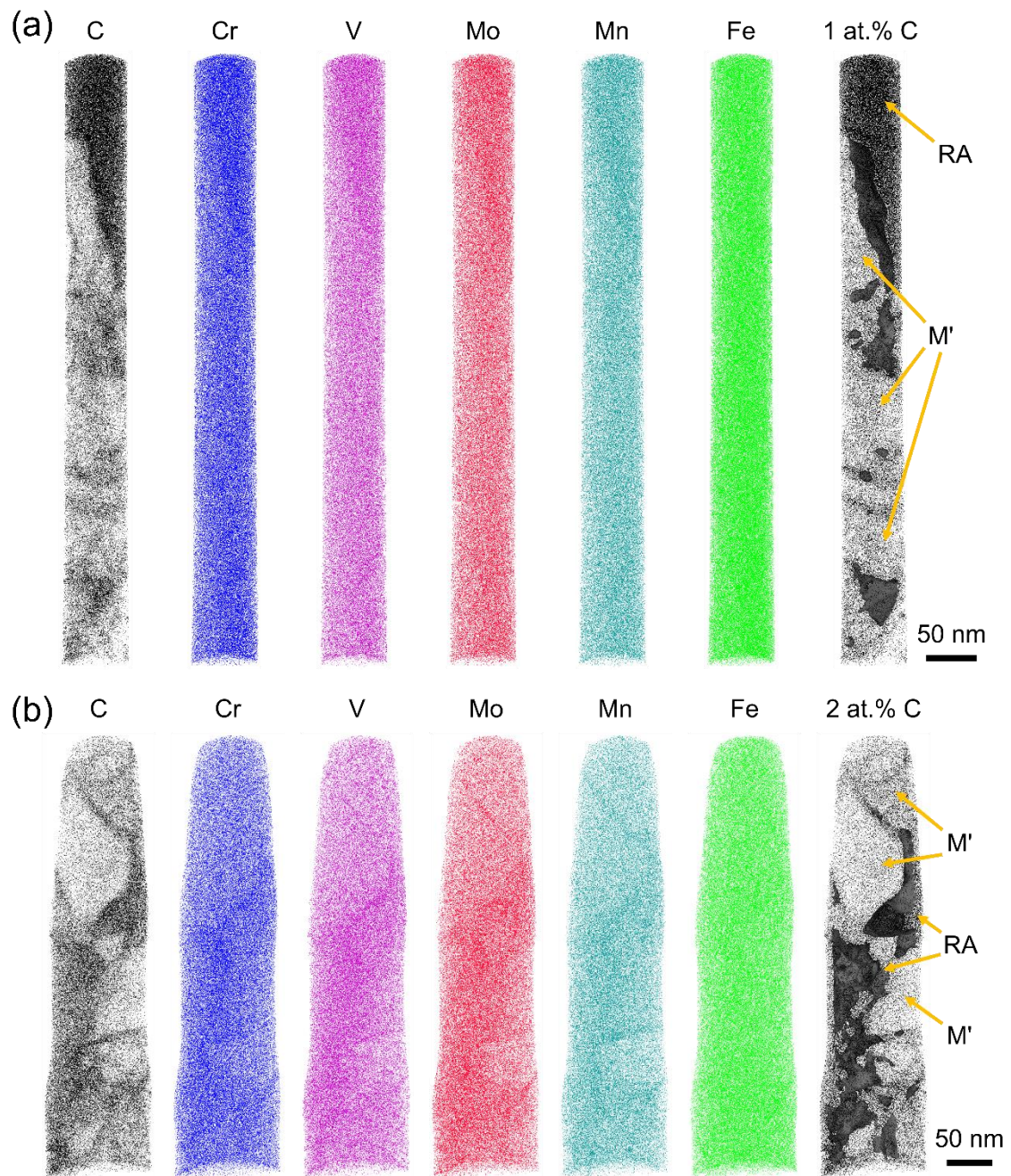
Fig. S4. Atom probe tomography ion maps and carbon isosurfaces for representative samples of (a) as-built, and (b) tempered at 575°C AISI H13 tool steel. M': martensite, RA: retained austenite.
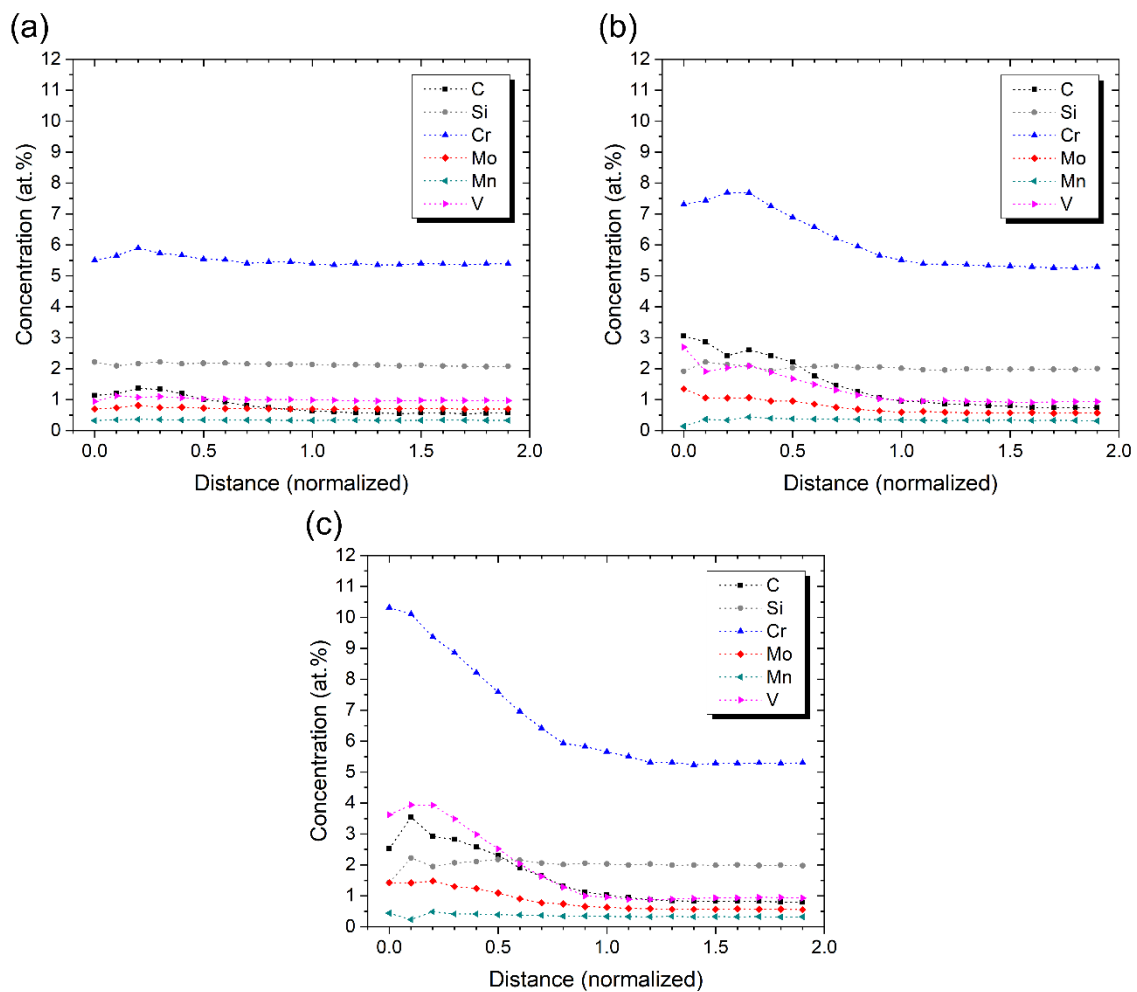
Fig. S5. Cluster concentration profiles for carbon clusters in (a) as-built and (b) tempered at 575°C conditions, and (c) for vanadium clusters in the tempered condition. Cluster search performed in martensitic regions of the APT tips. The distance in the composition profiles is normalized so that 0 corresponds to the center of the clusters, and 1 to the outer surface of the clusters; values larger than 1 correspond to the martensitic matrix.